SPECIAL
C4MIP
COLLECTION

Drake Passage Oceanic pCO_2: Evaluating CMIP5 Coupled Carbon–Climate Models Using in situ Observations

CHUANLI JIANG

Earth & Space Research, Seattle, Washington

SARAH T. GILLE AND JANET SPRINTALL

Scripps Institution of Oceanography, University of California, San Diego, La Jolla, California

COLM SWEENEY

CIRES, NOAA/ESRL/GMD, Boulder, Colorado

(Manuscript received 3 August 2012, in final form 21 August 2013)

ABSTRACT

Surface water partial pressure of CO_2 (pCO_2) variations in Drake Passage are examined using decade-long underway shipboard measurements. North of the Polar Front (PF), the observed pCO_2 shows a seasonal cycle that peaks annually in August and dissolved inorganic carbon (DIC)–forced variations are significant. Just south of the PF, pCO_2 shows a small seasonal cycle that peaks annually in February, reflecting the opposing effects of changes in SST and DIC in the surface waters. At the PF, the wintertime pCO_2 is nearly in equilibrium with the atmosphere, leading to a small sea-to-air CO_2 flux.

These observations are used to evaluate eight available Coupled Model Intercomparison Project, phase 5 (CMIP5), Earth system models (ESMs). Six ESMs reproduce the observed annual-mean pCO_2 values averaged over the Drake Passage region. However, the model amplitude of the pCO_2 seasonal cycle exceeds the observed amplitude of the pCO_2 seasonal cycle because of the model biases in SST and surface DIC. North of the PF, deep winter mixed layers play a larger role in pCO_2 variations in the models than they do in observations. Four ESMs show elevated wintertime pCO_2 near the PF, causing a significant sea-to-air CO_2 flux. Wintertime winds in these models are generally stronger than the satellite-derived winds. This not only magnifies the sea-to-air CO_2 flux but also upwells DIC-rich water to the surface and drives strong equatorward Ekman currents. These strong model currents likely advect the upwelled DIC farther equatorward, as strong stratification in the models precludes subduction below the mixed layer.

1. Introduction

The global ocean takes up more than a quarter of the total anthropogenic carbon dioxide (CO_2) that is released into the atmosphere, and the Southern Ocean is thought to be responsible for more than 40% of the global ocean's uptake of anthropogenic CO_2 (e.g., Toggweiler and Samuels 1995; Orr et al. 2001; Sarmiento et al. 2004; Russell et al. 2006; Marinov et al. 2006; Mikaloff Fletcher et al. 2006). Southern Ocean net uptake of anthropogenic and natural CO_2 is thus an important factor controlling future CO_2 levels in the atmosphere. Fluxes of CO_2 through the air–sea interface are controlled by winds and by differences in the partial pressure of CO_2 (pCO_2) in the surface ocean compared with the overlying atmosphere (e.g., Takahashi et al. 2002). Since geographical variations of atmospheric pCO_2 are relatively small (Conway et al. 1994; Takahashi et al. 2002), temporal and spatial variations of Southern Ocean pCO_2 are key to assessing projections for future atmospheric CO_2 concentrations (e.g., Marinov et al. 2008; Cadule et al. 2010).

Variations of surface water pCO_2 are governed by surface ocean temperature, salinity, dissolved inorganic carbon (DIC), and alkalinity (Alk). Surface ocean

---

Corresponding author address: ChuanLi Jiang, Earth & Space Research, 2101 4th Ave., Suite 1310, Seattle, WA 98121.
E-mail: chjiang@esr.org

DOI: 10.1175/JCLI-D-12-00571.1

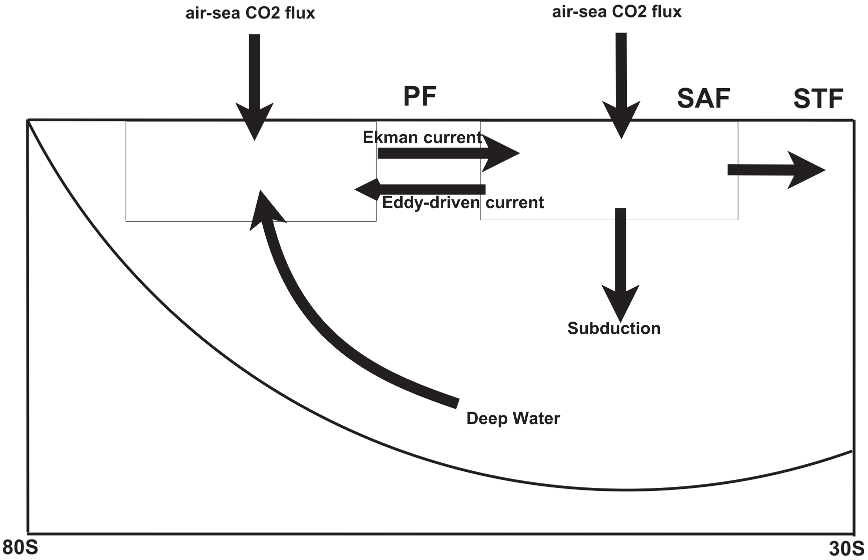

FIG. 1. Schematic of the overturning circulation in the Southern Ocean (Atlantic sector). At the PF, the upper layer is formed by the equatorward Ekman current and the poleward eddy-driven current (Speer et al. 2000; Iudicone et al. 2011). The deep water upwells DIC-rich water to the surface ocean south of the PF. North and south of the PF, the ocean takes up CO_2 from the overlying atmosphere, as indicated from the shipboard measurements. Also shown are the Subantarctic Front (SAF) and Subtropical Front (STF).

temperature and salinity are controlled by the coupled ocean–atmosphere physical processes. DIC and alkalinity are controlled by the air–sea gas exchange, horizontal and vertical transport, and mixing, as well as biological processes (e.g., Sarmiento and Gruber 2006). Surface water $p\mathrm{CO}_2$ is therefore determined by a complex interplay of biological, chemical, and physical processes.

Recent studies have shown that, since 1990, $p\mathrm{CO}_2$ in the surface waters of the Southern Ocean has increased at a rate that is similar to or slightly faster than the mean atmospheric rate of increase (e.g., Le Quéré et al. 2007; Lenton et al. 2012). Natural CO_2 is outgassed to the atmosphere in the westerly driven upwelling region of the Southern Ocean (e.g., Mikaloff Fletcher et al. 2007; Lovenduski et al. 2007). Takahashi et al. (2009) and Lovenduski et al. (2007, 2008), among others, have speculated that the strong poleward shift of the westerly winds since the 1960s, which is associated with the positive index of the southern annular mode, has produced stronger upwelling at and south of the fronts in the Antarctic Circumpolar Current (ACC) system. This strong poleward shift of the winds has also brought DIC-rich water from the deep ocean to the surface (see the schematic in Fig. 1). This hypothesis suggests that the total amount of DIC upwelled to the ocean surface south of the fronts and its location after being upwelled play a key role in predicting the CO_2 uptake rate by the Southern Ocean. A poleward shift of the fronts would reduce the area over which upwelling occurs and, together with the increased upwelling velocity, would likely change the total DIC in the Southern Ocean (Russell et al. 2006). The upper 1000 m of the ACC have warmed during the last 50–60 yr (e.g., Gille 2008), which would be expected to have increased seawater $p\mathrm{CO}_2$ and decreased oceanic CO_2 uptake. Furthermore, net cross-frontal transport, which is largely wind-driven equatorward Ekman transport but is partly compensated by the eddy-driven poleward transport, is expected to export upwelled DIC equatorward (Ito et al. 2009). These processes in the Southern Ocean are intimately tied to the global ocean through the meridional overturning circulation (Speer et al. 2000; Iudicone et al. 2011; Downes et al. 2011; D. C. Jones et al. 2011). Thus, examining the north–south variations of the Southern Ocean surface $p\mathrm{CO}_2$ is a key step toward understanding $p\mathrm{CO}_2$ variations associated with long-term climate change.

As a choke point of the ACC system, the Drake Passage has become a key location for investigating the Southern Ocean and its role in global climate. The decade-long (2002–11) underway surface water $p\mathrm{CO}_2$ measurements in Drake Passage (Takahashi et al. 2009; Sprintall et al. 2012) provide valuable in situ observations for examining $p\mathrm{CO}_2$ variations in this otherwise undersampled region. Given the importance of the Southern Ocean surface water $p\mathrm{CO}_2$ variations to the global carbon cycle, using the available in situ measurements to evaluate the Drake Passage $p\mathrm{CO}_2$ concentrations in the Coupled Model Intercomparison Project,

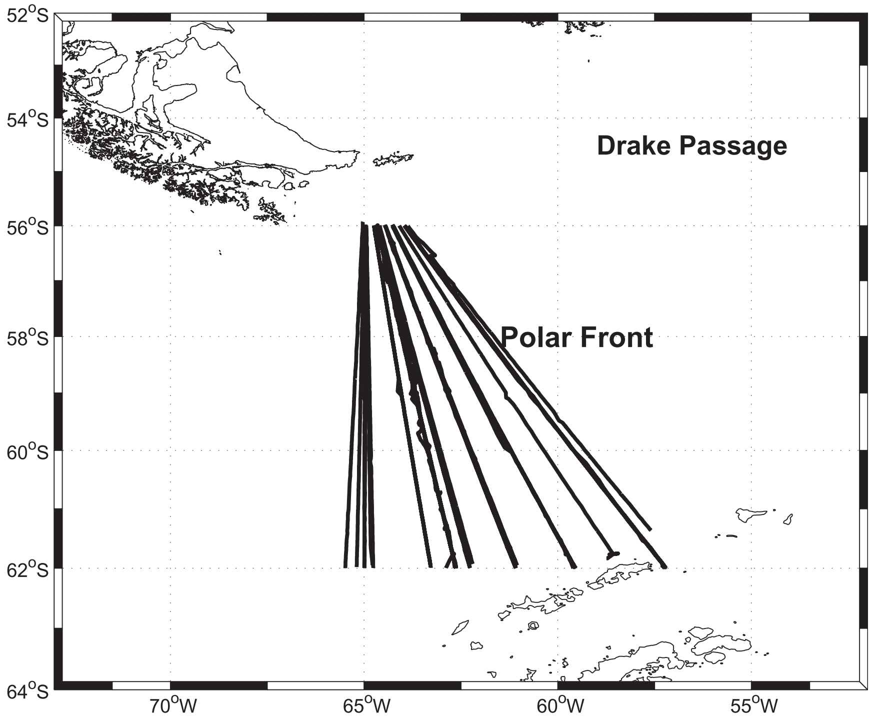

FIG. 2. The cruise tracks of 111 shipboard transects (black lines) in the Drake Passage from 2002 to 2011. Note that the mean Polar Front is located around 58.5°S. The Drake Passage region in this study is defined as the triangle covered by these 111 transects, with vertices at 56°S, 65°W; 62°S, 65°W; and 62°S, 57°W.

phase 5 (CMIP5) Earth system models (ESMs) will help to assess projections of future atmospheric concentrations. In earlier coupled model intercomparisons, the majority of ESMs prescribed CO_2 concentration scenarios, derived from relatively simple offline carbon cycle models (Friedlingstein et al. 2006). In CMIP5, the ESMs couple the ocean carbon cycle to the climate models (Fung et al. 2000; Cox et al. 2002; Friedlingstein et al. 2006).

In this study, we first examine the spatial mean, meridional, and seasonal variations of the underway decade-long (2002–11) shipboard $p\mathrm{CO}_2$ measurements across Drake Passage. We then use these in situ measurements to evaluate $p\mathrm{CO}_2$ variations in eight CMIP5 ESMs that were available for this study (Taylor et al. 2012). To further investigate discrepancies between the observations and the ESMs, we also compare the westerly winds, ocean currents, and stratification between the models and the satellite and in situ measurements. We found that six of the eight CMIP5 ESMs show spatial-mean surface water $p\mathrm{CO}_2$ concentrations that are comparable to shipboard measurements in the Drake Passage. The seasonal cycles of all ESMs except one, however, have larger seasonal cycles than the observations. Moreover, in the Polar Front region, four of the eight ESMs simulate seawater partial pressures that are elevated by 15–60 μatm relative to atmospheric partial pressures, resulting in a significant sea-to-air CO_2 flux to the overlying atmosphere.

2. Observations and CMIP5 ESMs

The ice-strengthened Antarctic support ship R/V *Laurence M. Gould* traverses Drake Passage approximately 20 times per year through all seasons, taking about 2 days for each crossing. Since March 2002, the ship has measured surface water $p\mathrm{CO}_2$ with an underway sampling frequency of 2.5 min. As of March 2011, 178 transects had been completed. Of these, we selected 111 transects that have relatively straight trajectories for direct comparison with the gridded ESM results (Fig. 2). This quality control approach for selecting transects is similar to that used by Jiang et al. (2012) in a study of turbulent heat fluxes. In this study, we refer to the Drake Passage region as the triangle covered by these 111 transects, with vertices at 56°S, 65°W; 62°S, 65°W; and 62°S, 57°W (Fig. 2).

Seawater $p\mathrm{CO}_2$ was measured using a showerhead equilibration method (Takahashi et al. 2002). The seawater was equilibrated continuously with a carrier gas in this water–air equilibrator. The equilibrated air samples were then dried, and the seawater CO_2 concentration was determined every 2.5 min. The reproducibility of measurements of the dry mole fraction [moles of CO_2 (moles)$^{-1}$ of dry air] in the atmospheric samples taken every 2 h have been evaluated by direct comparison with discrete flask measurements taken as the ship crosses the Polar Front on each cruise (roughly every 15 days) in the Drake Passage. Both flask and underway measurements were taken from the same inlet line mounted on the bow mast of the *Gould*. The flasks were then measured by National Oceanic and Atmospheric Administration (NOAA)/Earth System Research Laboratory (ESRL) using standards whose mole fractions are directly linked to the World Meteorological Organization. Since the strong westerly winds result in the atmospheric pCO$_2$ being well mixed across the Drake Passage, in the following analysis we will use the discrete flask measurement as representative of atmospheric pCO$_2$ across the whole passage. Comparisons between the discrete and underway measurements yielded differences of less than 0.15 μatm. Given temperature corrections and other artifacts associated with converting the dry mole fraction of CO_2 in air to pCO$_2$ in surface seawater, we estimate the accuracy of the pCO$_2$measurements to be $\pm 1\,\mu$tam. Temperatures were measured at 4 m from a thermosalinograph on the *Gould* to help assess the temporal and spatial variations in oceanic pCO$_2$. In this study, these 4-m shipboard ocean temperatures will be referred to as sea surface temperatures (SSTs). The SST precision is estimated to be about 0.005°C.

As noted above, CMIP5 Earth system models are directly coupled to ocean carbon models (Taylor et al. 2012). The model design of the coupled carbon–climate models in CMIP5 is based on CMIP3 (Fung et al. 2000; Cox et al. 2002; Friedlingstein et al. 2006). For this analysis we focus on the time period from 2002 to 2011. The first part of this period, from 2002 to 2005, is considered historical in the CMIP5 simulations. For the period from 2006 to 2011, we use the representative concentration pathway (RCP) 8.5 scenario, which is defined such that the radiative forcing of all direct and indirect agents reaches 8.5 W m^{-2} near 2100 (http://www.pik-potsdam.de/~mmalte/rcps/). We use results from eight climate modeling groups selected because, as of May 2012, they offered the only ESMs that provided surface water pCO$_2$ output for historical and RCP 8.5 experiments. The eight climate modeling groups are 1) the Beijing Climate Center Climate System Model, version 1.1 (BCC_CSM1.1; Wu et al. 2013); 2) the second generation Canadian Earth System Model (CanESM2; Arora et al. 2011; Zahariev et al. 2008); 3) the Hadley Centre Global Environment Model, version 2–Earth System (HadGEM2-ES; C. D. Jones et al. 2011; Collins et al. 2011), 4) the Institute of Numerical Mathematics Climate Model, version 4.0 (INM-CM4.0; Volodin et al. 2010); 5) the Model for Interdisciplinary Research on Climate, Earth System Model (MIROC-ESM; Watanabe et al. 2011), 6) the Max Planck Institute Earth System Model, low resolution (MPI-ESM-LR; Raddatz et al. 2007; Marsland et al. 2003; Ilyina et al. 2013); 7) the Geophysical Fluid Dynamics Laboratory Earth System Model with Generalized Ocean Layer Dynamics (GOLD) component (GFDL-ESM2G; Dunne et al. 2012); and 8) the Geophysical Fluid Dynamics Laboratory Earth System Model with Modular Ocean Model 4 (MOM4) component (GFDL-ESM2M; Dunne et al. 2013). The Program for Climate Model Diagnosis and Intercomparison (PCMDI) at Lawrence Livermore National Laboratory (http://www-pcmdi.llnl.gov/) provides some documentation for these ESMs.

In general, with typical resolution of 2° × 2°, most of the CMIP5 models represent the effects of eddies using eddy parameterizations (e.g., Gent and McWilliams 1990). However, as summarized by Gnanadesikan et al. (2006), GFDL-ESM2M uses the skew flux approach of Griffies (1998), in which the quasi-Stokes streamfunction is computed (Ferrari et al. 2010). These models also differ in the bathymetry dataset they used. For instance, BCC_CSM1.1 used the 5-min digital bathymetric database and MIROC-ESM used a spatially smoothed ETOPO5 topography. In contrast to the smoothed ETOPO5 topography used in GFDL-ESM2M, GFDL-ESM2G uses a depth average of the high-resolution ETOPO5 bathymetry (Dunne et al. 2012). The bathymetry used in HadGEM2-ES is derived from the ETOPO5 1/12° at high latitudes (Johns et al. 2006).

Although the majority of the ESMs do not restore the ocean surface tracers (temperature, salinity, and alkalinity) to the climatologies, these models differ in the specification of their ocean biogeochemistry. For instance, GFDL-ESM2G and GFDL-ESM2M include all elemental cycles, including limiting nutrients (nitrogen, phosphorus, iron, and silicate) and other substances cycled by the biosphere (carbon, oxygen, lithic material, calcium carbonate, opal, and sulfur). These two models also include three explicit phytoplankton classes—small, large, and diazotrophs—comprising four phytoplankton functional types: small, nitrogen fixers, large nondiatom, and large diatom. HadGEM2-ES includes carbon, oxygen, iron, and sulfur cycles and two phytoplankton classes (diatoms and nondiatoms). In CanESM2 and MIROC-ESM, only carbon and nitrogen cycles and one phytoplankton class (single species) are included. Carbon, oxygen, and phosphorus cycles and no phytoplankton class are included in BCC_CSM1.1. MPI-ESM-LR includes carbon, nitrogen, oxygen, and phosphorus cycles and one phytoplankton class with a diagnostic discrimination between diatoms and coccolithophores. INM-CM4.0 has only the carbon cycle and no phytoplankton class. These model differences in the quantification of the model ocean biogeochemistry are expected to result in differences in model performance in representing the ocean biogeochemical cycles.

We use a sampling strategy similar to that of Jiang et al. (2012), who compared shipboard transects of turbulent flux-related variables to gridded flux products. Gridded CMIP5 ESMs provide synoptic Eulerian maps, while shipboard measurements are not strictly synoptic. Thus, we linearly interpolate the gridded CMIP5 ESM output to the longitude, latitude, and time of the ship observations along the 111 transects used in this study. To evaluate the mechanisms governing model–data $p\mathrm{CO}_2$ differences, in addition to $p\mathrm{CO}_2$ and air-to-sea CO_2 flux, we examine three physical variables in both the CMIP5 ESMs and in the observational fields: surface currents, westerly winds, and stratification.

For this study, near-surface (30 m) currents are from the 5-day, $\frac{1}{3}^\circ \times \frac{1}{3}^\circ$ Ocean Surface Current Analyses–Real Time (OSCAR) from 2002 to 2009, which uses scatterometer-derived vector winds to compute the wind-driven velocity from an Ekman/Stommel formulation (Lagerloef et al. 1999; Bonjean and Lagerloef 2002; Dohan et al. 2010; Dohan and Maximenko 2010). The end date is determined by the fact that Quick Scatterometer (QuikSCAT) winds are not available after November 2009. OSCAR uses the gradient of ocean surface topography fields from an altimetric gridded Archiving, Validation, and Interpretation of Satellite Oceanographic (AVISO) data product (http://www.aviso.oceanobs.com). OSCAR also includes a contribution from horizontal temperature gradients using the Reynolds objectively interpolated SST product (OI.v2; Reynolds and Smith 1994), which influences velocity via the thermal wind relation. The drifter currents from the Global Drifter Program (Lumpkin and Pazos 2007) and the time–space interpolated OSCAR currents indicate correlation coefficients greater than 0.8 (K. Dohan 2012, personal communication).

We compare CMIP5 ESM winds with wind fields from the four times daily $1^\circ \times 1^\circ$ Center for Ocean-Atmospheric Prediction Studies (COAPS) QuikSCAT wind speed from 2002 to 2009 (Q-COAPS; Pegion et al. 2000). Wind speed at 10 m for Q-COAPS uses a direct minimization approach with tuning parameters determined from generalized cross-validation and QuikSCAT satellite observations filtered by the normalized objective function rain flag. We selected Q-COAPS winds rather than ship winds to evaluate the winds in CMIP5 ESMs for three primary reasons. One reason stems from the high regression slope (0.71 ± 0.17) and correlation coefficient (0.75 ± 0.16) between the QuikSCAT level 2B swath winds at 25-km resolution (which Q-COAPS uses to produce the gridded fields) and the 1-min-interval shipboard wind measurements in the Drake Passage (Jiang et al. 2012). The second reason is that the gridded winds are less noisy and can provide large spatial coverage compared to the ship measurements. Finally, OSCAR relies on the Q-COAPS winds and so, for consistency, we use the same.

Finally to evaluate the vertical stratification of CMIP5 ESMs and its possible links with the surface water $p\mathrm{CO}_2$, we use monthly *World Ocean Atlas 2009* (*WOA09*) potential temperature calculated from temperature and salinity (Locarnini et al. 2010; Antonov et al. 2010) along 65°W. To examine the meridional variation of the seasonal cycle of mixed layer depths (MLDs), we also use the surface ocean MLDs derived from the expendable conductivity–temperature–depth (XCTD) sampling in Drake Passage (Sprintall 2003; Stephenson et al. 2012). This MLD is defined as the depth at which potential density differs from the potential density at 11-m depth by $0.03\ \mathrm{kg\ m^{-3}}$ (e.g., Stephenson et al. 2012). To examine the MLD variation over a broader zonal extent within the Drake Passage region, we use climatological MLDs derived from Argo float measurements (Holte et al. 2010; Holte and Talley 2009).

3. Drake Passage variations

In this section, we investigate the variations of seawater $p\mathrm{CO}_2$ and related variables in the Drake Passage using the decade-long shipboard measurements. We then use these measurements to evaluate the overall performance of the eight CMIP5 ESMs.

a. Time mean

Bias and standard error of the 111-transect-averaged seawater $p\mathrm{CO}_2$ from eight CMIP5 ESMs relative to the shipboard measurements are shown in Fig. 3a (gray bars). Positive values indicate that in the spatial average, model estimates exceed observed values. In the Drake Passage, six out of the eight CMIP5 ESMs show a spatially averaged time-mean bias smaller than $6\ \mu\mathrm{atm}$. Among these six ESMs, $p\mathrm{CO}_2$ values in BCC_CSM1.1, GFDL-ESM2G, and GFDL-ESM2M underestimate the Drake Passage's $p\mathrm{CO}_2$ by up to $6\ \mu\mathrm{atm}$, while the $p\mathrm{CO}_2$ values in CanESM2, INM-CM4.0, and MIROC-ESM overestimate by up to $4\ \mu\mathrm{atm}$. The other two ESMs, HadGEM2-ES and MPI-ESM-LR, underestimate the surface ocean $p\mathrm{CO}_2$ by 25 and $19\ \mu\mathrm{atm}$, respectively.

In addition to the annual means (gray bars), Fig. 3a also shows seasonal-mean biases for austral winter

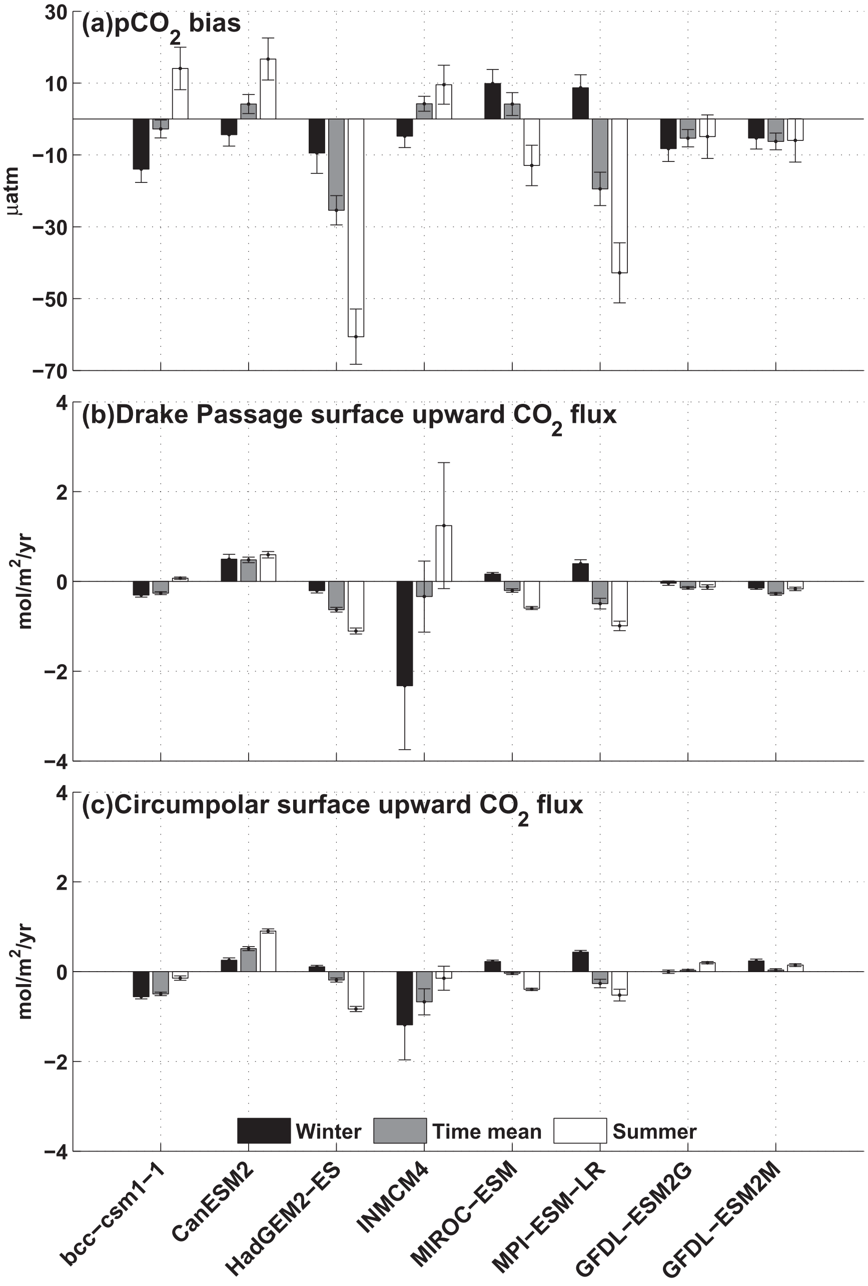

FIG. 3. (a) Bias and standard error of the difference of transect-averaged seawater pCO_2 from eight CMIP5 ESMs relative to shipboard measurements. Differences between the ESMs and shipboard measurements are shown in the austral winter (July–September; black bars), time mean (gray bars), and summer (January–March; white bars). Positive values in (a) indicate overestimation compared to the shipboard measurements. (b) The mean and standard error of transect-averaged surface upward sea-to-air CO_2 flux from the eight CMIP5 ESMs. (c) As in (b), but for surface upward sea-to-air CO_2 flux averaged in the entire circumpolar region (56°–62°S). No shipboard measurements are available for the surface upward CO_2 flux. Positive values in (b),(c) indicate upward CO_2 flux from the ocean to the overlying atmosphere. The standard error equals the standard deviation divided by square root of the number of the transects.

(July–September; black bars) and austral summer (January–March; white bars). These seasons are chosen because they represent extremes in surface $p\mathrm{CO}_2$ (see section 3b). For the eight CMIP5 ESMs, the winter $p\mathrm{CO}_2$ biases are less than 14 μatm, with GFDL-ESM2M, CanESM2, and INM-CM4.0 underestimating the winter $p\mathrm{CO}_2$ by up to 5 μatm. While HadGEM2-ES and MPI-ESM-LR have the largest time-mean biases (19–25 μatm) in Drake Passage, their winter biases are less than 10 μatm. Their summer biases, however, are larger than 40 μatm. The summer biases for the other six ESMs are less than 17 μatm.

The net CO_2 flux out of the ocean F is a function of the sea-to-air $p\mathrm{CO}_2$ difference $\delta p\mathrm{CO}_2$, the CO_2 gas transfer velocity k, and the solubility of CO_2 in seawater α, $F = k\alpha\delta p\mathrm{CO}_2$ (Sweeney et al. 2007; Takahashi et al. 2009). At fixed temperature and salinity, the gas transfer velocity k is thought to be roughly a power function of wind speed: that is, $k \propto U^x$, where U is wind speed and x has been proposed to have a value between 1 (Liss and Merlivat 1986) and 3 (Wanninkhof and McGillis 1999). The *Gould* does not directly measure the air–sea CO_2 flux, and its estimation depends on interpolating not only the $p\mathrm{CO}_2$ (which changes slowly) but also synoptic winds (which change rapidly); therefore, comparing monthly air–sea fluxes with in situ values is not straightforward. In addition, its estimation through the bulk algorithm described above (Sweeney et al. 2007; Takahashi et al. 2009), using the measured $p\mathrm{CO}_2$ and the other available data products, results in large variations and uncertainties. This further complicates the evaluation of the CMIP5 model performance. Hence, in the following we present only an intermodel comparison of the sea-to-air CO_2 flux from the eight CMIP5 ESMS (Fig. 3b) with no comparison to the CO_2 flux estimated using the bulk algorithm. Positive values represent the upward CO_2 flux into the atmosphere. In the time mean (gray bars), GFDL-ESM2G has the smallest air–sea CO_2 flux in the Drake Passage. CanESM2 fluxes CO_2 into the overlying atmosphere, while in the other seven CMIP5 ESMs the ocean takes up CO_2 from the overlying atmosphere. During the austral winter period, however, two of these seven ESMs (MIROC-ESM and MPI-ESM-LR) release CO_2 into the overlying atmosphere.

To examine the extent to which the results found in the Drake Passage (Fig. 3b) represent the entire circumpolar region, we show in Fig. 3c the sea-to-air CO_2 flux averaged in the entire circumpolar region (56°–62°S) from eight CMIP5 ESMs. In both the annual and seasonal means, the sea-to-air CO_2 flux in the entire circumpolar region compares well with the CO_2 flux in the Drake Passage, implying that the Drake Passage's $p\mathrm{CO}_2$ variations are representative of the entire circumpolar region.

b. *Seasonal cycle*

From the previous subsection, we know that six of the eight CMIP5 ESMs show spatially averaged surface water $p\mathrm{CO}_2$ values that are comparable to the shipboard measurements in Drake Passage (with time-mean biases smaller than 6 μatm). We now examine the seasonal cycles by fitting the observations and constructed ESM transects to a sinusoidal seasonal cycle using a least squares approach.

Examining the seasonal variations of seawater $p\mathrm{CO}_2$ requires examining its dependent variables. As discussed earlier, surface water $p\mathrm{CO}_2$ depends on surface temperature, salinity, DIC, and alkalinity. That is, $p\mathrm{CO}_2 \approx K_2/(K_0K_1)(2\mathrm{DIC} - \mathrm{Alk})^2/(\mathrm{Alk} - \mathrm{DIC})$, where $K_2/(K_0K_1)$ is the equilibrium constant, which is a function of temperature and salinity. To investigate SST-forced surface ocean $p\mathrm{CO}_2$ changes, we compute the effect of SST on $p\mathrm{CO}_2$ by perturbing the mean $p\mathrm{CO}_2$ with the difference between the observed and mean temperature (Takahashi et al. 2002). That is, $p\mathrm{CO}_2|_{\mathrm{SST}} \approx \overline{p\mathrm{CO}_2}\exp[0.0423(\mathrm{SST} - \overline{\mathrm{SST}})]$, where $\overline{p\mathrm{CO}_2}$ and $\overline{\mathrm{SST}}$ are the time-mean $p\mathrm{CO}_2$ and temperature. Since salinity-forced seasonal $p\mathrm{CO}_2$ variations are negligible (Sarmiento and Gruber 2006), we interpret the residual component after subtracting the SST-forced $p\mathrm{CO}_2$ changes as $p\mathrm{CO}_2$ changes forced by DIC and alkalinity, $p\mathrm{CO}_2|_{\mathrm{DIC,Alk}} = p\mathrm{CO}_2 - p\mathrm{CO}_2|_{\mathrm{SST}}$. Alkalinity is more homogeneous than DIC in Drake Passage, with a typical fixed value of 2268 μmol kg^{-1}, as empirically estimated by McNeil et al. (2007). As a result, $p\mathrm{CO}_2|_{\mathrm{DIC,Alk}}$ is mainly controlled by DIC variations, and henceforth we refer to it as $p\mathrm{CO}_2|_{\mathrm{DIC}}$.

Figure 4a shows the seasonal cycles of the seawater $p\mathrm{CO}_2$ from the shipboard measurements and eight CMIP5 ESMs. The observed Drake Passage–averaged seawater $p\mathrm{CO}_2$ (thick black line) is highest in austral winter (August) and lowest in austral summer (February). Note that the time-mean $p\mathrm{CO}_2$ value (368 μatm) is included in Fig. 4a, and the summer-to-winter change clearly shows the seasonal variations of $p\mathrm{CO}_2$ (Table 1). Positive signs in Table 1 indicate that the peak month occurs in austral winter, and negative signs indicate the peak month is in austral summer. Observed $p\mathrm{CO}_2$ increases 9 μatm from a minimum in austral summer to a maximum in winter (Fig. 4a), as a result of the compensation between the SST-forced $p\mathrm{CO}_2$ drawdown of 51.0 μatm (Fig. 4b) and the DIC-forced $p\mathrm{CO}_2$ increase of 60.3 μatm (Fig. 4c). SST-forced seasonal $p\mathrm{CO}_2$ variations are approximately 6 months out of phase with DIC-forced $p\mathrm{CO}_2$ changes both for the observations and for the eight CMIP5 ESMs: SST-forced $p\mathrm{CO}_2$ changes reach their highest values in austral summer, and DIC-forced $p\mathrm{CO}_2$ are highest in austral winter

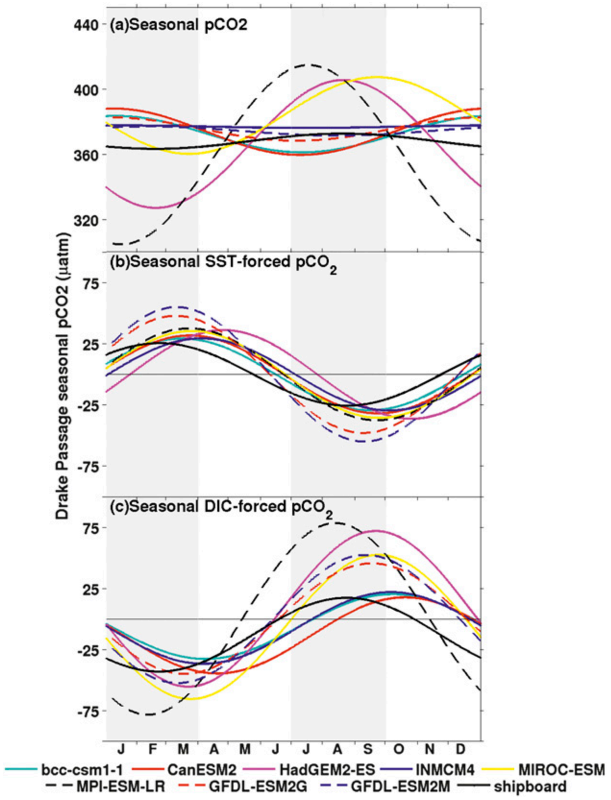

FIG. 4. Seasonal cycles of the 111-transect seawater $p\mathrm{CO_2}$ and its related variables from eight CMIP5 ESMs and shipboard measurements in Drake Passage. The variables include (a) seawater $p\mathrm{CO_2}$, (b) SST-forced seawater $p\mathrm{CO_2}$ computed from the temperature sensitivity of $p\mathrm{CO_2}$, and (c) DIC-forced seawater $p\mathrm{CO_2}$ computed by differencing (a) and (c). Gray shading denotes the austral summer period from January to March and winter period from July to September.

TABLE 1. The summer-to-winter magnitudes of the seawater $p\mathrm{CO_2}$, the SST-forced $p\mathrm{CO_2}$ change ($p\mathrm{CO_2}|_{\mathrm{SST}}$), and the DIC-forced changes ($p\mathrm{CO_2}|_{\mathrm{DIC}}$) for the shipboard measurements and eight CMIP5 ESMs. Positive values indicate $p\mathrm{CO_2}$ increase from the austral winter (July–September) to the austral summer (January–March).

	$p\mathrm{CO_2}$ (μatm)	$p\mathrm{CO_2}|_{\mathrm{SST}}$ (μatm)	$p\mathrm{CO_2}|_{\mathrm{DIC}}$ (μatm)
Ship	9.3	−51.0	60.3
BCC_CSM1.1	−22.3	−58.5	52.9
CanESM2	−28.4	−63.5	62.2
HadGEM2-ES	78.4	−72.3	127.1
INM-CM4.0	1.5	−58.7	60.3
MIROC-ESM	47.0	−70.7	117.7
MPI-ESM-LR	109.8	−74.9	156.5
GFDL-ESM2G	−14.4	−95.5	90.2
GFDL-ESM2M	−5.6	−109.6	104.6

when wintertime mixing with DIC-rich deep waters and respiration of organic matter have peaked.

Four of the eight CMIP5 ESMs (HadGEM2-ES, INM-CM4.0, MIROC-ESM, and MPI-ESM-LR) are consistent with shipboard measurements in showing high $p\mathrm{CO_2}$ values in austral winter (positive signs). However, three of these four ESMs (HadGEM2-ES, MIROC-ESM, and MPI-ESM-LR) have much larger summer-to-winter $p\mathrm{CO_2}$ differences than the observations. These large summer-to-winter differences stem mainly from the fact that DIC-forced seasonal $p\mathrm{CO_2}$ changes dominate SST-forced seasonal $p\mathrm{CO_2}$ changes (Table 1). Consistent with this finding, Cadule et al. (2010) used an atmospheric transport model in conjunction with output from three ESMs (including a previous version of HadGEM2-ES) and found larger seasonal air–sea flux variations in the Southern Ocean than the station observations. The other four CMIP5 ESMs (CanESM2, BCC_CSM1.1, GFDL-ESM2G, and GFDL-ESM2M) are 6 months out of phase with the shipboard measurements, largely because SST-forced $p\mathrm{CO_2}$ changes in these models dominate DIC-forced $p\mathrm{CO_2}$ changes (Table 1).

Figure 5 shows the seasonal cycles of the entire circumpolar (56°–62°S) seawater $p\mathrm{CO_2}$ and its related variables ($p\mathrm{CO_2}|_{\mathrm{SST}}$ and $p\mathrm{CO_2}|_{\mathrm{DIC}}$) from the eight CMIP5 ESMs. The seasonal cycles of the SST- and DIC-forced $p\mathrm{CO_2}$ changes in the entire circumpolar region (Figs. 5b,c) in all ESMs significantly correlate with the $p\mathrm{CO_2}$ changes in the Drake Passage (Figs. 4b,c), with correlation coefficients above 0.85. The entire circumpolar $p\mathrm{CO_2}$ variations (Fig. 5a) in six of the eight ESMs significantly correlate with the variations in the Drake Passage (Fig. 4a), with correlation coefficients above 0.83. The exceptions are INM-CM4.0 ($R = 0.66$, $R_{95\%\mathrm{CI}} = 0.72$) and GFDL-ESM2M ($R = 0.12$, $R_{95\%\mathrm{CI}} = 0.75$), mainly because their peak months in the Drake Passage $p\mathrm{CO_2}$ variations greatly differ from their peak months in the circumpolar region.

c. Anomalies

The previous two subsections show that the time mean (Fig. 3) and seasonal cycles (Fig. 5) of seawater $p\mathrm{CO_2}$ in Drake Passage largely represent the entire circumpolar region in most of the eight ESMs. To further examine the extent to which the $p\mathrm{CO_2}$ variations in Drake Passage resemble the other areas of the circumpolar region, we show in Fig. 6 the spatial (lag) correlations of the 10°-longitude-averaged seawater $p\mathrm{CO_2}$ anomalies for the circumpolar region (56°–62°S) with the Drake Passage–averaged (57°–67°W) $p\mathrm{CO_2}$ anomalies for eight CMIP5 ESMs. The $p\mathrm{CO_2}$ anomalies here are obtained by removing the time mean, the long-term trend, and the seasonal cycles from the original time series. In calculating the correlation coefficients in Fig. 6, we take the time series of the $p\mathrm{CO_2}$ averaged in Drake Passage and

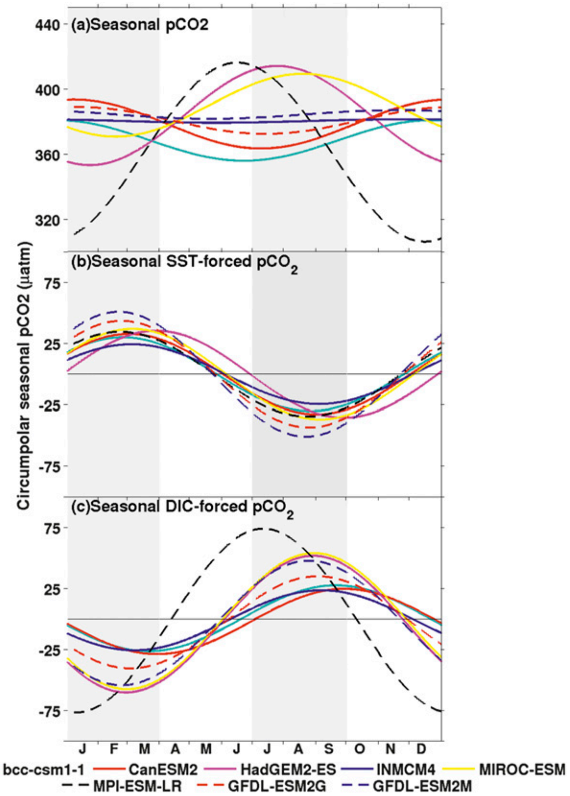

FIG. 5. As in Fig. 4, but for the seasonal cycles of the entire circumpolar (56°–62°S) seawater $p\mathrm{CO}_2$ and its related variables from eight CMIP5 ESMs.

correlate it at zero time lag with the $p\mathrm{CO}_2$ time series at other 10°-longitude bands around the Southern Ocean.

In general, the Drake Passage $p\mathrm{CO}_2$ anomalies significantly correlate with the other areas of the Southern Ocean for all ESMs. Surface water $p\mathrm{CO}_2$ anomalies from 56° to 62°S in INM-CM4.0 shows little longitudinal variations, including a fixed dominant linear trend and several fixed low frequencies, and the Drake Passage $p\mathrm{CO}_2$ anomalies therefore highly correlate with the other circumpolar areas (Fig. 6d). The little zonal variations in INM-CM4.0 are likely due to the fact that there is no biology in its ocean biogeochemistry. These findings, in conjunction with the results in the time mean and seasonal cycles as detailed in the previous two subsections, confirm the representativeness of the Drake Passage in the surface water $p\mathrm{CO}_2$ variations in the entire circumpolar region from 56° to 62°S for most of the eight ESMs.

4. Meridional variations

In this section we examine the meridional variations of the surface water $p\mathrm{CO}_2$, sea-to-air CO_2 flux, and the $p\mathrm{CO}_2$ seasonal cycles in the Drake Passage. We then use these observations to evaluate meridional variations of $p\mathrm{CO}_2$ in the eight CMIP5 ESMs.

The Polar Front, one of the major frontal features that defines the ACC, has a mean latitude around 58.5°S in Drake Passage (Sprintall 2003; Jiang et al. 2012). Differences in SST-forced and DIC-forced processes are observed north and south of the Polar Front (Takahashi et al. 2002; Downes et al. 2011; Iudicone et al. 2011). Given the importance of SST and DIC in the oceanic $p\mathrm{CO}_2$ variations (section 3b), seawater $p\mathrm{CO}_2$ is also expected to differ on either side of the Polar Front. As discussed in the introduction, examining the meridional variations of the Southern Ocean $p\mathrm{CO}_2$ is a key step toward understanding $p\mathrm{CO}_2$ variations associated with long-term climate change. Therefore, the relative roles of DIC- and SST-forced $p\mathrm{CO}_2$ variations north and south of the Polar Front are crucial to the projections of the future atmospheric CO_2 levels in the CMIP5 ESMs. With a typical resolution of 2° × 2°, however, these CMIP5 ESMs generally only have a few grid points in the Drake Passage region and thus do not have sufficient resolution to allow a full evaluation of their meridional gradients. The evaluations in this section help define requirements for future improvements of these CMIP5 ESMs.

Here we refer to the region 57.5°–59.5°S as the Polar Front, the region 56°–57.5°S as north of the Polar Front, and the region 59.5°–62°S as south of the Polar Front. These regional definitions are for descriptive purposes only, as the Polar Fronts in the CMIP5 ESMs are not consistently located around 58.5°S because of model biases that may stem in part from coarse model resolution. Because of this, we show in Figs. 7 and 8 the meridional variation of surface $p\mathrm{CO}_2$ and sea-to-air CO_2 flux with respect to SST instead of latitude. This removes biases in the Polar Front position but shows biases in temperature and meridional gradients, reflecting a range of processes that contribute to $p\mathrm{CO}_2$ and sea-to-air CO_2 flux variations. We also examine westerly winds, surface ocean currents, and potential temperature profiles in order to probe the data–model discrepancies.

a. Seawater pCO_2

During austral winter, biological consumption is low and physical processes dominate $p\mathrm{CO}_2$ variability. We thus show only data from the austral winter period between July and September in sections 4a–4c. The impact of biological consumption on seasonal $p\mathrm{CO}_2$ variations will be addressed in section 4d. In Fig. 7, we plot constructed wintertime oceanic $p\mathrm{CO}_2$ against SST for the eight ESMs and the shipboard observations: $p\mathrm{CO}_2$ values north of the Polar Front are shown as red, near

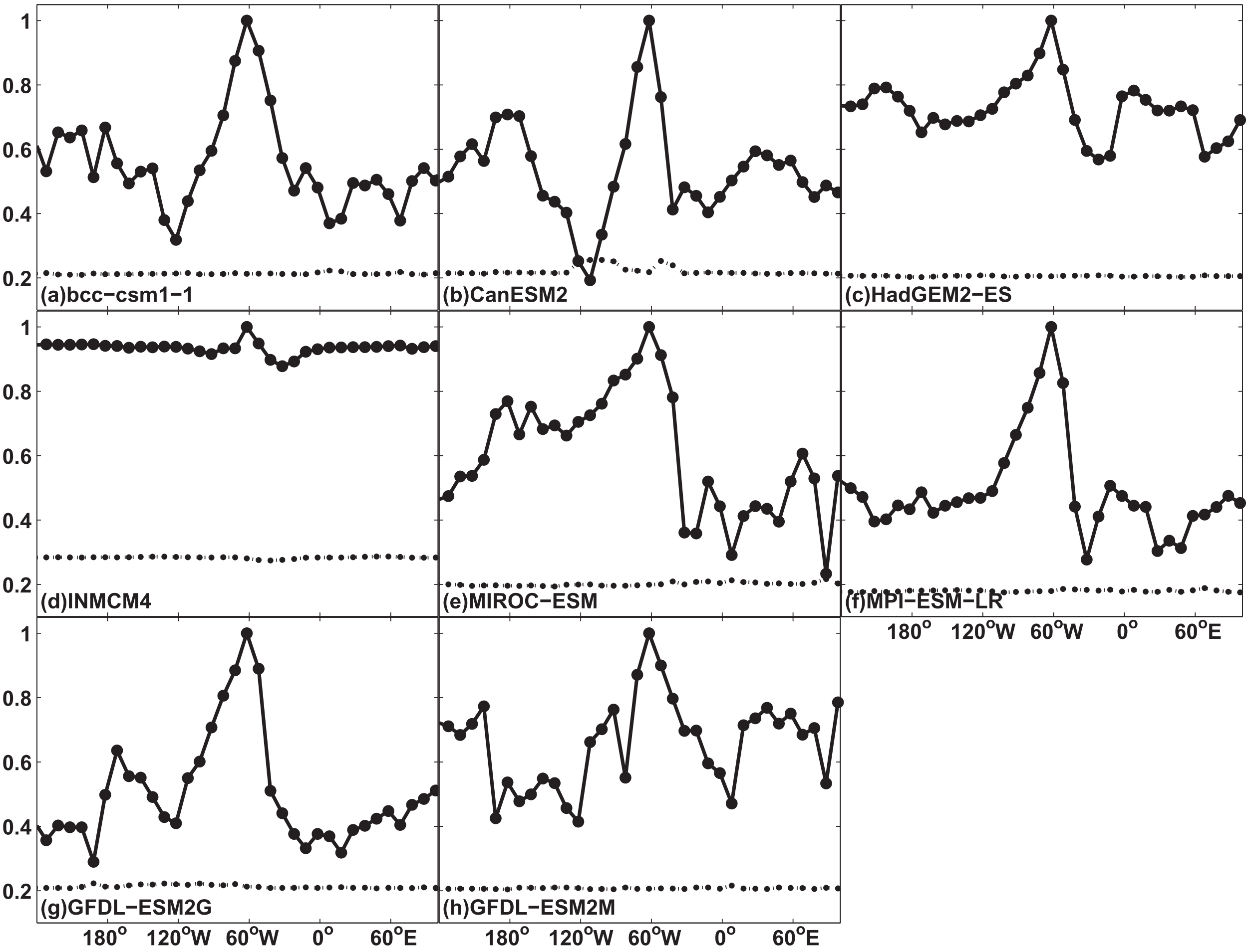

FIG. 6. Spatial (lag) correlations of 10°-longitude-averaged seawater $p\mathrm{CO}_2$ anomalies along the circumpolar region (from 56° to 62°S) with the Drake Passage–averaged (57°–67°W) $p\mathrm{CO}_2$ anomalies for eight CMIP5 ESMs. The $p\mathrm{CO}_2$ anomalies are obtained by removing the time mean, the long-term trend, and the seasonal cycles. The dotted lines show the 95% significance level correlation values.

the Polar Front are shown as black, and south of the Polar Front are shown as magenta. The 0.3°C SST-binned averages of $p\mathrm{CO}_2$ as a function of SST are shown as the thick black lines with the error bars denoting the standard error of the mean. In computing the degrees of freedom, each transect is treated as an independent realization, because the transects cover all seasons of the year with consecutive transects typically separated in time by 2–6 weeks and each transect takes about 2 days to complete.

As noted above, the strong westerly winds in the ACC system tend to homogenize the atmospheric $p\mathrm{CO}_2$ in the planetary boundary layer, and so the discrete in situ atmospheric $p\mathrm{CO}_2$ (Fig. 7i) is considered representative of atmospheric $p\mathrm{CO}_2$ variations across the entire Drake Passage. Similarly, the atmospheric $p\mathrm{CO}_2$ concentrations in the eight ESMs also show little meridional variation (cyan lines in Figs. 7a–h). Note that the discontinuous cyan lines in GFDL-ESM2G and GFDL-ESM2M (Figs. 7g,h) are due to the missing data near the ice edge in the Southern Ocean.

The shipboard observations (Fig. 7i) show that the winter-averaged surface water $p\mathrm{CO}_2$ near the Polar Front (2°–4°C; 385 μatm; thick black line) is nearly in equilibrium with the time-mean atmospheric $p\mathrm{CO}_2$ (380 μatm). The observed atmospheric $p\mathrm{CO}_2$ values increase with time from 2002 to 2011 (cyan lines in Fig. 7i). The atmospheric $p\mathrm{CO}_2$ growth rate is estimated to be 1.95 $\mu\mathrm{atm\,yr}^{-1}$, close to the growth rate of 1.9 $\mu\mathrm{atm\,yr}^{-1}$ in the Southern Ocean reported by Lenton et al. (2012). The growth rate of the spatially averaged observed oceanic $p\mathrm{CO}_2$ is estimated to be 2.4 $\mu\mathrm{atm\,yr}^{-1}$, close to previous reported values of 2.5 ± 0.7 $\mu\mathrm{atm\,yr}^{-1}$ by Lenton et al. (2012) and 2.2 ± 0.5 $\mu\mathrm{atm\,yr}^{-1}$ by Takahashi et al. (2009). Although the decadal-mean surface water $p\mathrm{CO}_2$ is nearly in equilibrium with the decadal-mean atmospheric $p\mathrm{CO}_2$, over the 10-yr

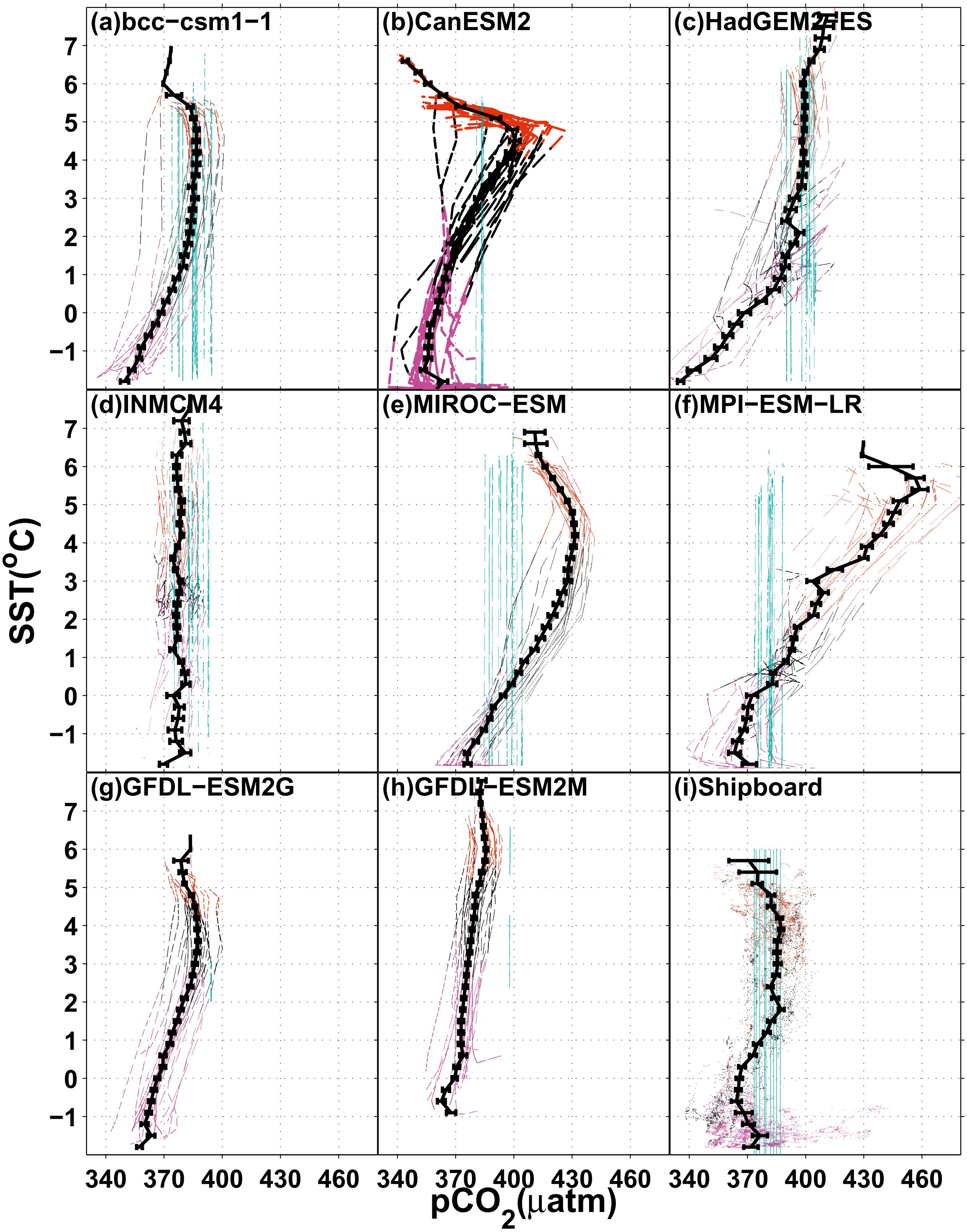

FIG. 7. July–September constructed seawater $p\mathrm{CO_2}$ against SST for (a)–(h) eight CMIP5 ESMs and (i) the shipboard observations in the Drake Passage region. Data points north of the Polar Front (56°–57.5°S) are shown in red, near the Polar Front (57.5°–59.5°S) are shown in black, and south of the Polar Front (59.5°–62°S) are shown in magenta. The thick black lines show the 0.3°C SST-binned averages of $p\mathrm{CO_2}$ as a function of SST, and the error bars denote the standard error of the mean. The multiple thick cyan lines in (a)–(h) show the constructed atmospheric $p\mathrm{CO_2}$ along the winter transects in eight ESMs and in (i) show the observed atmospheric $p\mathrm{CO_2}$ in Drake Passage by NOAA/ESRL for the years 2003–11.

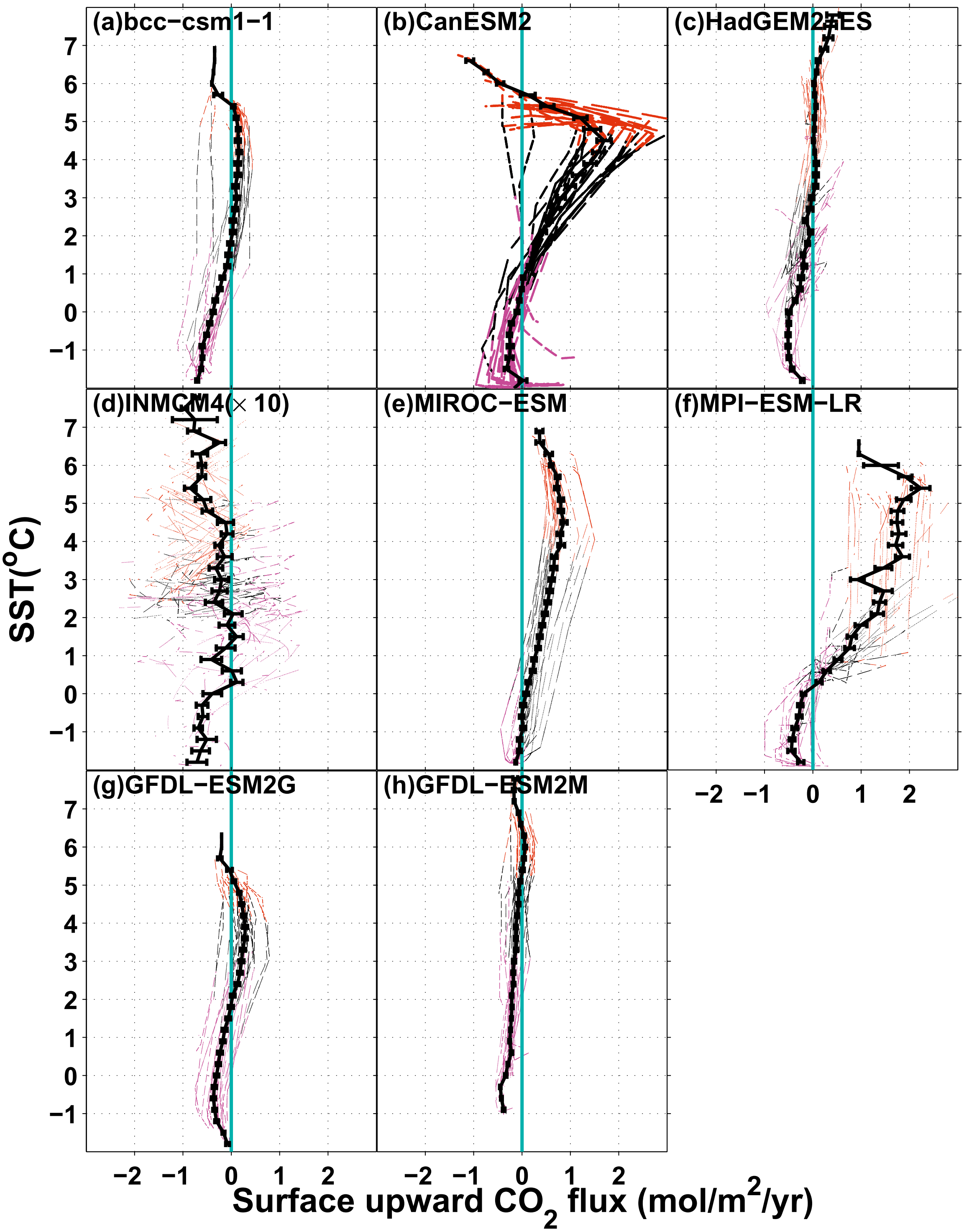

FIG. 8. As in Fig. 7, but for July–September sea-to-air CO_2 flux (mol m^{-2} yr^{-1}) against SST. Positive values indicate sea-to-air upward CO_2 flux.

time series the growth rate of the ocean pCO_2 increases faster compared to that of the atmospheric pCO_2. This faster oceanic growth rate means that sea-to-air fluxes of CO_2 are higher by the end of the time series in 2011.

The region just south of the Polar Front (SST < -1°C) has lower seawater pCO_2 concentrations (360 μatm) than the overlying atmosphere (Fig. 7i), indicating that the ocean acts as a sink for atmospheric CO_2 within the

Southern Ocean seasonal ice zone (Fig. 1). Sprintall et al. (2012) showed a strong correlation of $\delta p\mathrm{CO}_2$ and upper ocean temperature just south of the Polar Front (PF) in winter in the Drake Passage, suggesting that SST plays a role in seawater $p\mathrm{CO}_2$ variations there. From the equilibrium with the atmosphere at 2°C to the under saturation at −1°C, seawater $p\mathrm{CO}_2$ (thick black lines in Fig. 7i) decreases from 385 to 360 μatm. The SST dependence of seawater $p\mathrm{CO}_2$ (8 $\mu\mathrm{atm}\,{}^{\circ}\mathrm{C}^{-1}$) south of the Polar Front is half the SST dependence (16 $\mu\mathrm{atm}\,{}^{\circ}\mathrm{C}^{-1}$) that would be estimated based on the relation developed by Takahashi et al. (1993), who found $\delta p\mathrm{CO}_2/\delta \mathrm{SST} \approx 0.0423 \times p\mathrm{CO}_2$, assuming SST to be the sole factor controlling variations in $p\mathrm{CO}_2$. The fact that the observed seasonal cycle in $p\mathrm{CO}_2$ is less dependent on SST than predicted by its change in solubility implies that, south of the Polar Front, DIC-forced seawater $p\mathrm{CO}_2$ changes may also play an important role. The DIC-forced processes might include the air-to-sea CO_2 flux and the upwelling of high DIC water from the deep ocean, as indicated in Fig. 1.

North of the Polar Front, for SSTs around 6°C, observed seawater $p\mathrm{CO}_2$ is about 370 μatm, which is lower than in the Polar Front (385 μatm at 2°–4°C) and is a departure from equilibrium with the atmosphere. On the basis of temperature dependence alone, $p\mathrm{CO}_2$ would be expected to increase with warmer temperatures, so the observed departure from equilibrium has the wrong sign to be temperature controlled. This departure implies that the DIC sink terms, such as subduction into the deep ocean and uptake by phytoplankton, may play a significant role north of the Polar Front. Alternatively, source waters from the subtropics could contribute to lower DIC water, which, when cooled to 6°C, results in a significantly lower $p\mathrm{CO}_2$ than found at the Polar Front. Iudicone et al. (2011) argued that water mass transformations can have an important impact in setting the surface carbon properties north of the Polar Front. We speculate that the effective subduction into the deep ocean in the convergence zone, the wind-driven equatorward meridional transport, and the DIC uptake by photosynthesis likely play a role in removing carbon from surface water. This is due to the fact that other processes, such as air–sea gas flux and possible cross-frontal equatorward transport from the south, all should increase surface water $p\mathrm{CO}_2$ (Fig. 1).

Six of the eight ESMs are consistent with observations that show a maximum of seawater $p\mathrm{CO}_2$ near the Polar Front. The exceptions are INM-CM4.0 (Fig. 7d) and to a lesser extent HadGEM2-ES (Fig. 7c). All ESMs except INM-CM4.0 show a $p\mathrm{CO}_2$ reduction as temperatures decrease south of the Polar Front. However, in other respects, the eight available ESMs show significantly different meridional variations than the observations (Figs. 7a–h). While all ESMs except INM-CM4.0 and GFDL-ESM2M show larger values of oceanic $p\mathrm{CO}_2$ than in the overlying atmosphere near the Polar Front, the seawater $p\mathrm{CO}_2$ in four ESMs (CanESM2, MIROC-ESM, MPI-ESM-LR, and to some extent GFDL-ESM2G) appears to exceed atmospheric $p\mathrm{CO}_2$ values by 15–60 μatm, suggesting that the sea-to-air $p\mathrm{CO}_2$ gradients are larger in these four models than in the observations (Figs. 7b,e–g). If we assume the winds are the same in all ESMs and in the shipboard measurements (we will show in section 4c that the model winds are generally too strong), then the Polar Fronts in these four models lose much more CO_2 to the overlying atmosphere than suggested by the shipboard observations or the other ESMs because of the excessive sea-to-air gradient. The minimum values of $p\mathrm{CO}_2$ south of the Polar Front in these four models, however, are consistent with the shipboard measurements. This leads to a much larger south-to-north increase in $p\mathrm{CO}_2$ between the −1°C water south of the PF and the 4°C water near the Polar Front, implying excessive DIC sources by the oceanic physical processes near the Polar Front in these four models. These processes could include an overestimate in the upwelling of DIC-rich water and excessive biological drawdown of DIC as the waters move north of the PF or rapid mixing of subtropical waters before waters are subducted into the deep ocean, as indicated in Fig. 1. In addition, CanESM2 appears to have a narrower SST range (4°–5°C) over which the oceanic $p\mathrm{CO}_2$ is larger than the overlying atmosphere (Fig. 7b). This narrower SST range implies less total CO_2 uptake from the overlying atmosphere.

b. Sea-to-air CO_2 flux

Figure 8 shows austral winter transects of the CO_2 flux from the ocean to the atmosphere as a function of SST, where positive values indicate a sea-to-air CO_2 flux out of the ocean. The sea-to-air CO_2 flux in INM-CM4.0 (Fig. 8d) is about an order of magnitude larger than in the other ESMs. The meridional variations of sea-to-air CO_2 flux (Fig. 8) are generally proportional to the sea-to-air $p\mathrm{CO}_2$ differences (Fig. 7) for all ESMs, implying that in these models the air–sea $p\mathrm{CO}_2$ differences play an important role in the air–sea CO_2 flux.

Near the Polar Front, the oceans of four models (BCC_CSM1.1, HadGEM2-ES, INM-CM4.0, and GRDL-ESM2M; Figs. 8a,c,d,h) are nearly in equilibrium with the overlying atmosphere. In these models, the ocean acts as a sink for atmospheric CO_2 south of the Polar Front for water temperatures less than 1°C. In contrast, in CanESM2 (Fig. 8b), MIROC-ESM (Fig. 8e), MPI-ESM-LR (Fig. 8f), and to some extent GFDL-ESM2G (Fig. 8g), the oceans release CO_2 to the overlying atmosphere,

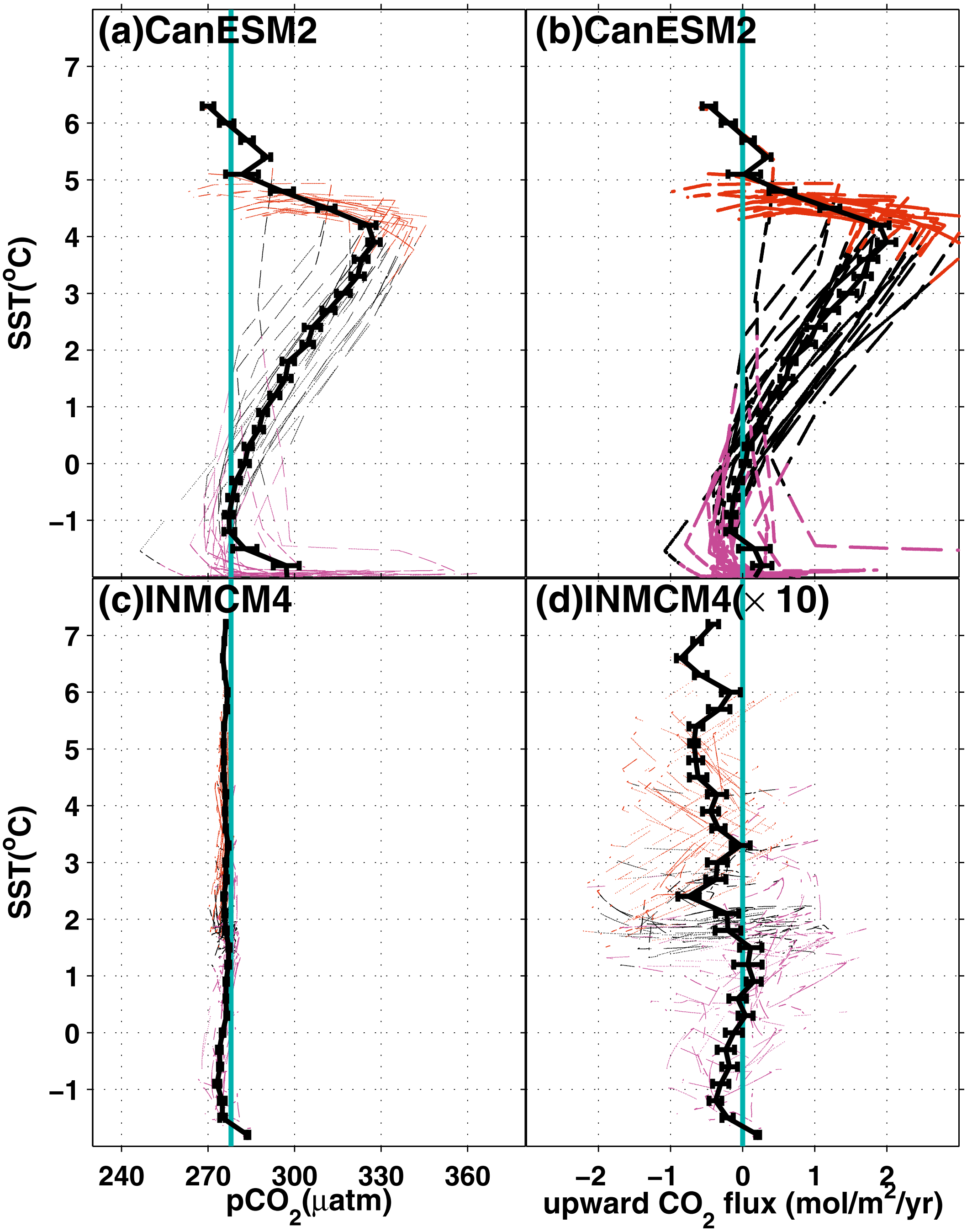

FIG. 9. July–September constructed seawater $p\text{CO}_2$ against SST for (a) CanESM2 and (c) INM-CM4.0 and sea-to-air CO_2 flux against SST for (b) CanESM2 and (d) INM-CM4.0 in the control experiment simulated with preindustrial atmospheric $p\text{CO}_2$ (278 μatm).

because seawater $p\text{CO}_2$ exceeds atmospheric $p\text{CO}_2$. In these same models south of the Polar Front, oceanic $p\text{CO}_2$ is nearly in equilibrium with the atmosphere, and as a result the oceans exchange little CO_2 with the overlying atmosphere. The near equilibrium state illustrated by the shipboard $p\text{CO}_2$ observations (Fig. 7i) at the Polar Front stands in contrast to these four ESMs that show a CO_2 source to the overlying atmosphere.

To further investigate the excessive sea-to-air CO_2 flux near the Polar Front, we show in Fig. 9 the oceanic $p\text{CO}_2$ and sea-to-air CO_2 flux for CanESM2 and INM-CM4.0 in the preindustrial control experiments. These two models are the only models that provide the oceanic $p\mathrm{CO}_2$ output for the ESM control experiments. In these control experiments, the oceanic $p\mathrm{CO}_2$ variations and air–sea CO_2 flux are merely driven by the natural carbon variation and flux, as constant preindustrial atmospheric $p\mathrm{CO}_2$ values (278 μatm) are used. As a result, the differences of $p\mathrm{CO}_2$ variations (Figs. 7, 9) and sea-to-air CO_2 flux (Figs. 8, 9) indicate the effect of anthropogenic carbon variations that are input into the ocean.

For both CanESM2 and INM-CM4.0, the natural $p\mathrm{CO}_2$ variations and air–sea natural carbon flux show a meridional variation similar to that seen under contemporary conditions. In particular, under preindustrial conditions, seawater $p\mathrm{CO}_2$ values in CanESM2 exceed atmospheric $p\mathrm{CO}_2$ values (278 μatm) by about 50 μatm (Fig. 9a), and the Polar Front CO_2 outgassing to the atmosphere is about $2\,\mathrm{mol\,m^{-2}\,yr^{-1}}$ (Fig. 9b). These variations are larger than values under contemporary conditions, with oceanic $p\mathrm{CO}_2$ exceeding atmospheric $p\mathrm{CO}_2$ by about 15 μatm (Fig. 7b) and the sea-to-air CO_2 flux estimated to be $1.5\,\mathrm{mol\,m^{-2}\,yr^{-1}}$ (Fig. 8b). This implies that in CanESM2, natural carbon outgassing plays a larger role (1.4–4 times) than anthropogenic carbon uptake in determining the excessive $p\mathrm{CO}_2$ bias.

We also examined longitudinal (east–west) variations of sea-to-air CO_2 flux for the entire Drake Passage region (50°–80°W, 52°–62°S) in the eight ESMs (not shown). Consistent with Fig. 8, the oceans of CanESM2, MIROC-ESM, MPI-ESM-LR, and GFDL-ESM2G release CO_2 to the atmosphere at a rate of 0.5–$1.5\,\mathrm{mol\,m^{-2}\,yr^{-1}}$ at all longitudes near the Polar Front. In contrast, the oceans of BCC_CSM1.1 and HadGEM2-ES take up CO_2 at a rate of $0.5\,\mathrm{mol\,m^{-2}\,yr^{-1}}$ at all longitudes. In addition, south of the Polar Front the oceans in BCC_CSM1.1 and HadGEM2-ES have a higher CO_2 uptake rate than they do near the Polar Front.

c. *Winds and ocean currents*

Figures 7 and 8 indicate that the sea-to-air $p\mathrm{CO}_2$ differences $\delta p\mathrm{CO}_2$ are large enough to play an important role in the sea-to-air CO_2 flux in all ESMs. In particular, for all winter transects from 2002 to 2011, the $p\mathrm{CO}_2$ values in four of the eight ESMs (CanESM2, MIROC-ESM, MPI-ESM-LR, and to some extent GFDL-ESM2G) near the Polar Front coincide with large CO_2 releases to the atmosphere. To illustrate the relative roles of ocean currents and winds in the sea-to-air CO_2 flux, in Figs. 10a–h we show the austral winter-mean wind speed and the near-surface (30 m) ocean currents in all eight ESMs. Winds are dynamically determined features in all the eight CMIP5 ESMs. In this study we time average the winter wind speeds and currents to be consistent with Figs. 7 and 8. For comparison, we show in Fig. 10i the austral winter-mean QuikSCAT wind speed (2002–09) and the austral winter-mean OSCAR ocean currents (2002–09) derived from satellite measurements.

West of 65°W, the wind speeds in CanESM2, INM-CM4.0, MIROC-ESM, and MPI-ESM-LR are on average 2–$3\,\mathrm{m\,s^{-1}}$ stronger than QuikSCAT winds; however, east of 65°W, winds in these models are 3–$4\,\mathrm{m\,s^{-1}}$ stronger than QuikSCAT winds. This stronger wind bias in coupled general circulation models has also been reported by Swart and Fyfe (2011) and by Russell et al. (2006). As suggested by the schematic in Fig. 1, the strong eastward winds in these models in the entire Drake Passage region may 1) enlarge the magnitude of the CO_2 release from the ocean to the atmosphere; 2) enhance upwelling of higher DIC from the deep ocean to the surface at and south of the Polar Front; and 3) drive the Ekman transport in the surface layer of the Southern Ocean strongly northward (to the left of the eastward winds), which also moves DIC-rich water northward. Observations and models suggest that, near the Polar Front, eddy-driven poleward transport compensates to some extent the equatorward Ekman transport (Böning et al. 2008; Ito et al. 2009). In coarse-resolution models, overly strong winds can disrupt this balance and drive a northward net meridional transport. North of the Polar Front where intermediate water forms through convective processes (Speer et al. 2000), meridional transport is expected to be small in the near-surface layer of the ocean. However, in the four models with stronger winds east of 65°W, the austral winter-mean Eulerian ocean surface currents are consistently equatorward and stronger throughout all of Drake Passage compared to the observations. This implies that the upwelled DIC-rich water from south of the Polar Front is likely transported farther equatorward in the surface layer instead of being subducted into the deep ocean, leading to a longer exchange time with the atmosphere. It also seems likely that because of the low resolution the poleward eddy-driven meridional currents in these models are too weak to compensate the strong equatorward Ekman currents.

Vertical stratification can serve as a measure of how easily water can be subducted or upwelled. For this study we use the vertical gradient of potential temperature as an approximate measure of stratification since more detailed stratification information, such as potential density, is not readily available from the ESMs. The impact of the salinity on the stratification needs further study, as salinity potentially plays an important role in the mixed layer calculation in the Southern Ocean (e.g., Stephenson et al. 2012). Compared to the *WOA09* climatology (Fig. 11i), vertical profiles of potential

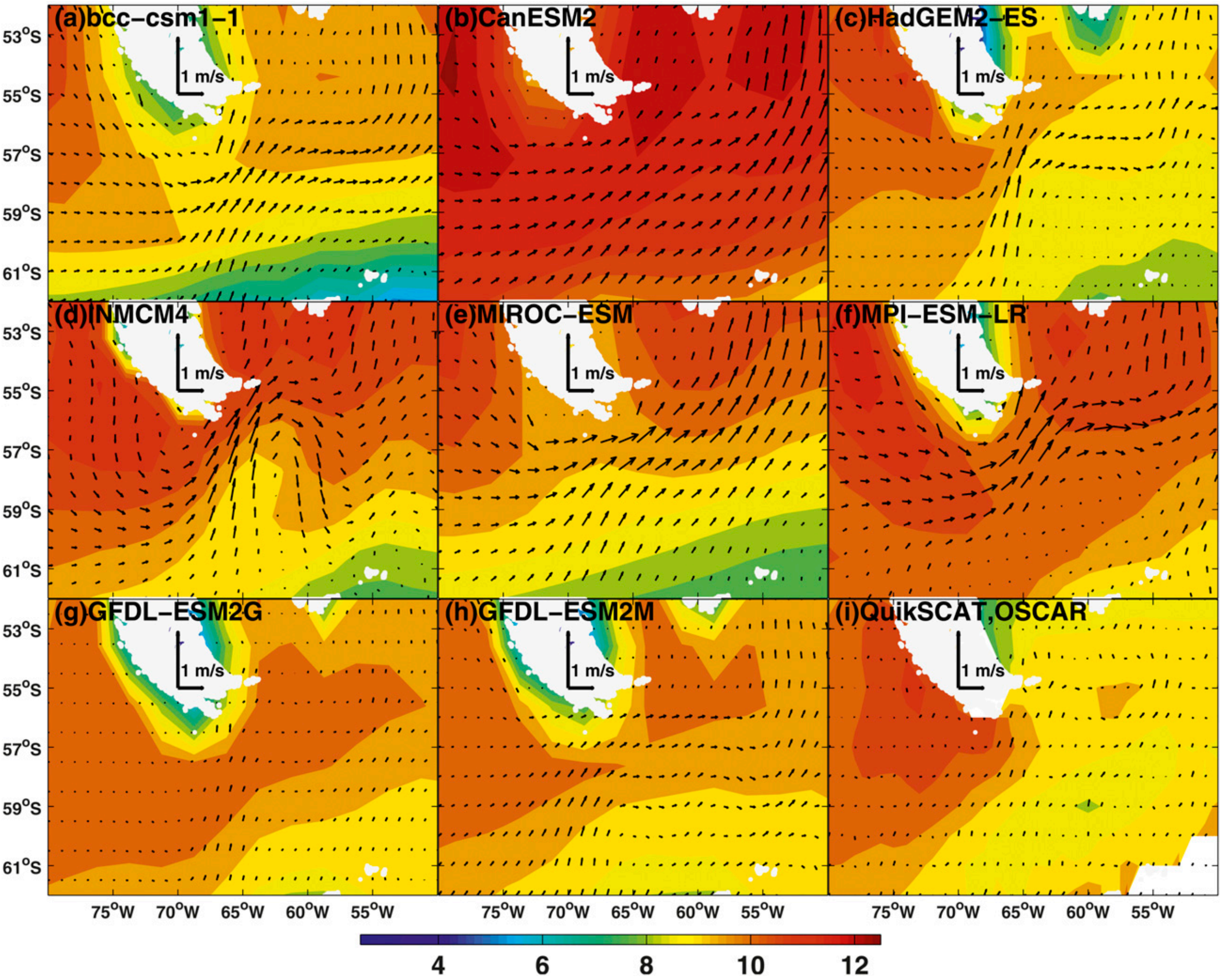

FIG. 10. (a)–(h) July–September-mean 10-m wind speeds (color; m s^{-1}) and the upper 30-m ocean currents (vectors) in the Drake Passage region (50°–80°W, 52°–62°S) for eight CMIP5 ESMs. (i) The QuikSCAT winds (2002–09) and OSCAR ocean currents (2002–09).

temperature along 65°W in CanESM2, HadGEM2-ES, INM-CM4.0, and MPI-ESM-LR (Figs. 11b–d,f) imply much stronger stratification at and just north of the Polar Front, making the upwelled DIC harder to subduct to the deep ocean in these regions. As shown in Fig. 1, four physical processes likely act together to reduce the model inventory of DIC in the Drake Passage. These processes include the strong westerly winds and the consequent strong equatorward Ekman transports, strong net meridional currents (implying weak poleward eddy transport compensation), strong stratification preventing subduction of CO_2 to the deep ocean, and excessive CO_2 flux to the atmosphere. A full analysis of the carbon budget in the Drake Passage would be needed to examine the effect of these physical processes on the DIC inventory in these models and is beyond the scope of this analysis.

d. *Seasonal cycle*

We now explore the relative roles of SST forcing and DIC forcing in governing the seasonal cycle of $p\mathrm{CO}_2$ as a function of meridional position within Drake Passage. We fitted the 1°-latitude-binned observations and the constructed ESM transects to a sinusoidal seasonal cycle (Fig. 12) using a least squares approach, $A\cos(2\pi t + \phi)$, where A and ϕ represent amplitude and phase. Here the amplitudes have positive sign and differ from the summer-to-winter magnitudes in Table 1, in which the magnitudes carry some of the phase information. Consistent with the Drake Passage–averaged results (Fig. 4 and Table 1), meridionally varying seawater $p\mathrm{CO}_2$ concentrations in the shipboard measurements and in all eight ESMs except INM-CM4.0 show a significant seasonal cycle. The amplitude of the seasonal cycle of

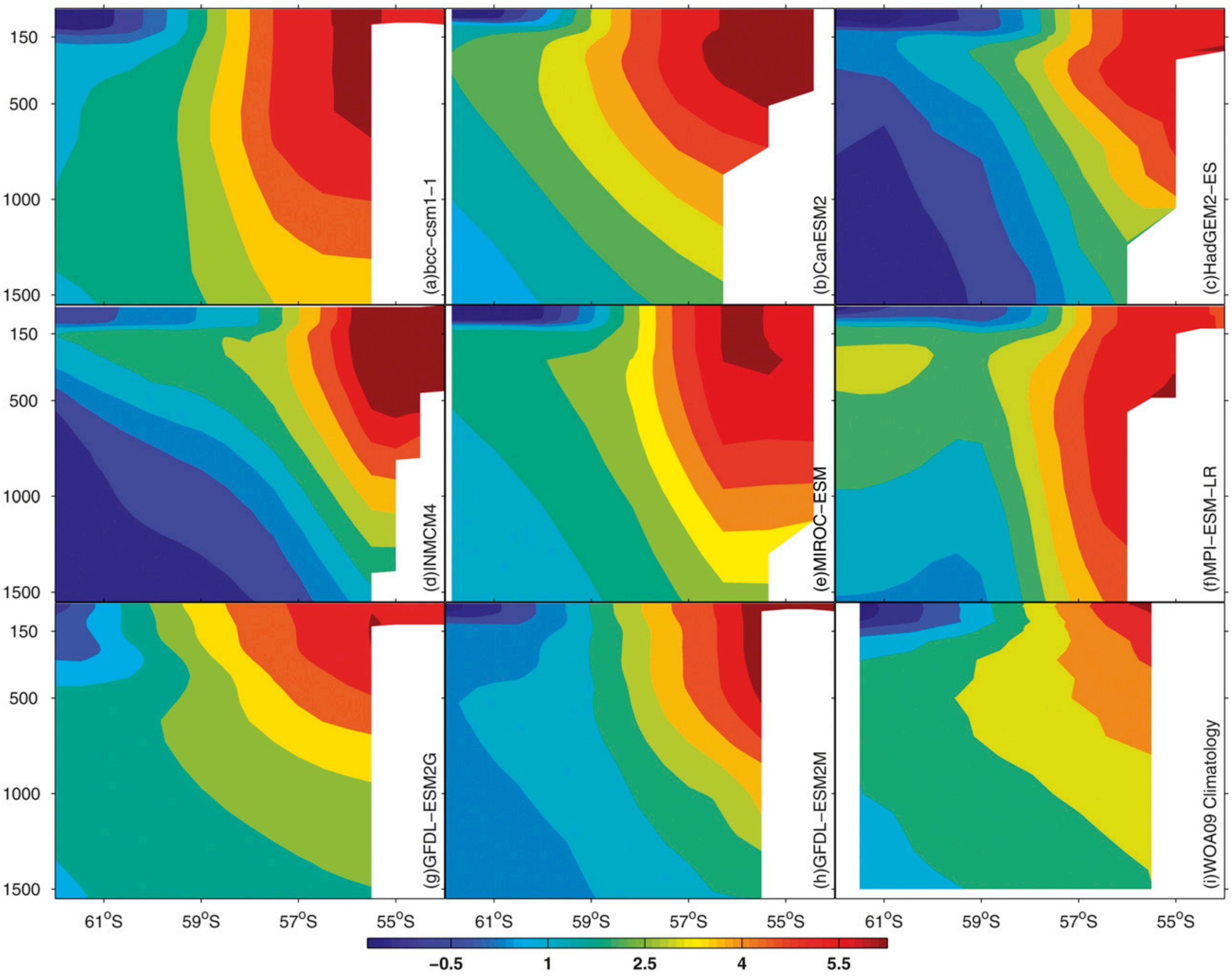

FIG. 11. Latitude–depth profiles of potential temperature (°C) along 65°W for eight CMIP5 ESMs and *WOA09* climatology.

observed $p\mathrm{CO}_2$ in the Drake Passage can reach up to 7.5 μatm, which is much smaller [$\mathcal{O}(10^{-1})$] than the seasonal $p\mathrm{CO}_2$ in other parts of the global ocean (Takahashi et al. 2009; Christian et al. 2010). In contrast, all of the ESMs, with the exception of INM-CM4.0, have much larger seasonal amplitudes (Fig. 12a). GFDL-ESM2G, GFDL-ESM2M, and BCC_CSM1.1 have seasonal cycle amplitudes for $p\mathrm{CO}_2$ that are most consistent with the shipboard measurements. The amplitude of the seasonal cycle of $p\mathrm{CO}_2$ in MPI-ESM-LR reaches up to 75 μatm at 56.5°S, and in HadGEM2-ES it reaches up to 47 μatm at 59.5°S.

The amplitudes of the seasonal cycles in surface water $p\mathrm{CO}_2$ show significant meridional variations (Fig. 12a, left). Just north of the Polar Front, the amplitude of the seasonal cycle of observed $p\mathrm{CO}_2$ is triple the amplitude south of the front (about 7.5 μatm compared to 2.5 μatm). Jiang et al. (2012) found the amplitude of the seasonal cycle of SST north of the Polar Front to be half the amplitude south of the front (about 1°C compared to 2°C). This suggests that the meridional gradients of the seasonal cycle amplitudes have opposite signs for $p\mathrm{CO}_2$ and SST. This confirms the results from the spatially averaged analysis that surface temperature is not the only factor controlling the seasonal cycle of the surface $p\mathrm{CO}_2$; DIC-related processes also contribute to seasonal variations in surface $p\mathrm{CO}_2$.

Like the amplitudes, the months when seawater $p\mathrm{CO}_2$ peaks vary with latitude (Fig. 12c). The observed seawater $p\mathrm{CO}_2$ consistently peaks in austral winter (August) north of the Polar Front and peaks in the austral summer (February) just south of the Polar Front. In the eight ESMs, $p\mathrm{CO}_2$ peaks between February and August; however, they differ greatly with latitude. In HadGEM2-ES, MIROC-ESM, and MPI-ESM-LR the phases of seawater $p\mathrm{CO}_2$ show little meridional variations and are mainly locked to austral winter. This agrees with the shipboard measurements north of the Polar

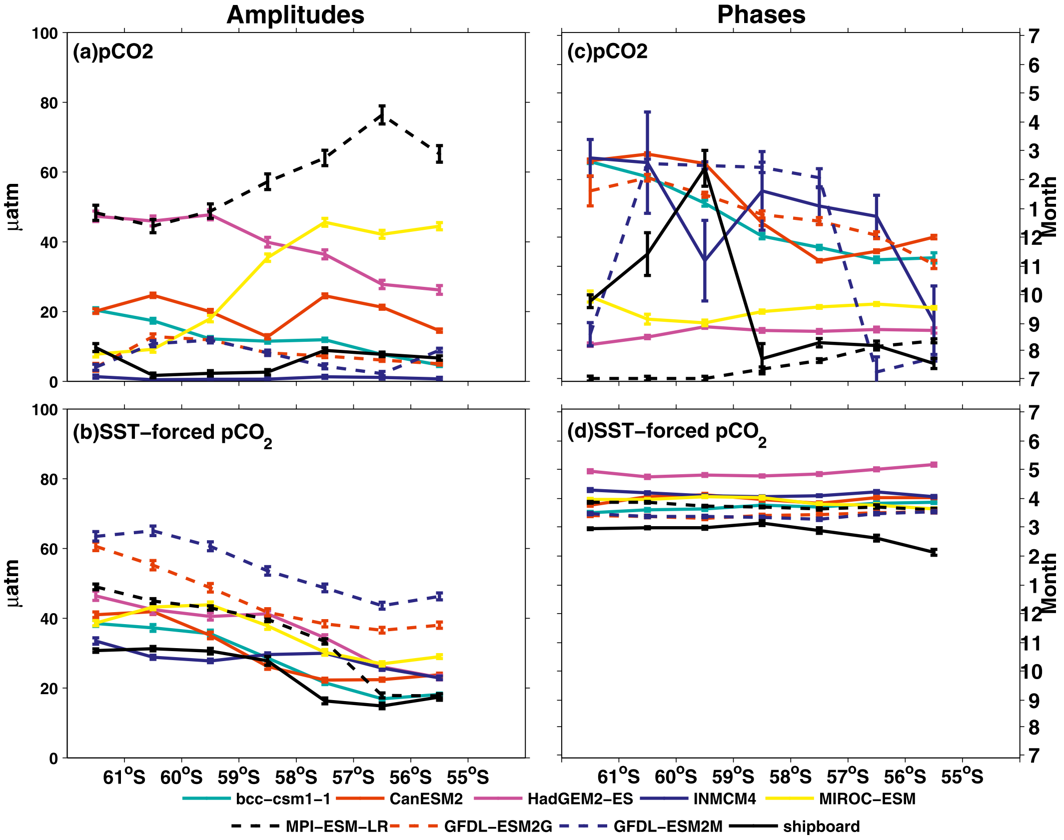

FIG. 12. (a),(b) Amplitudes and (c),(d) phases of (top) the seasonal cycles of surface water $p\mathrm{CO}_2$ and (bottom) the SST-forced component of surface $p\mathrm{CO}_2$, for the eight CMIP5 ESMs (see legend) and the in situ measurements (black solid). Error bars denote the standard error of the mean. The phases indicate the peak months of the seasonal cycles of surface water $p\mathrm{CO}_2$.

Front but not south of the Polar Front. In the models BCC_CSM1.1, CanESM2, and GFDL-ESM2G, the phases indicate a maximum between November and January north of the Polar Front, which is several months too late compared to the observations. Consistent with Woloszyn et al. (2011), the phases south of the Polar Front in the ESMs differ substantially from the observations, especially near the seasonally ice-covered regions (near 62°S). Overall, the meridional variation of the phase of $p\mathrm{CO}_2$ in GFDL-ESM2M best matches the observations but shows a gentler transition from south to north across the Polar Front, which is probably a result of the low horizontal resolution of the model.

We know from the spatially averaged seasonal cycle analysis in Fig. 4 that the compensation between the SST-forced and DIC-forced seasonal $p\mathrm{CO}_2$ changes determines the seasonal $p\mathrm{CO}_2$ variations. Further, Figs. 12b,d show the amplitudes and phases of the seasonal cycles of the $p\mathrm{CO}_2$ as predicted, based on the SST effect $p\mathrm{CO}_2|_{\mathrm{SST}}$. North of the Polar Front the amplitude of the seasonal cycles of $p\mathrm{CO}_2$ variations associated with SST is half the amplitude that it is south of the front (about 16 μatm to the north compared to 31 μatm to the south; Fig. 12b). This north–south gradient is by definition consistent with the seasonal cycles of SST (Jiang et al. 2012), but it is opposite to the seasonal cycles of oceanic $p\mathrm{CO}_2$ (Fig. 12a). While the amplitude of the seasonal cycle is larger in the eight ESMs compared to the observations, the meridional gradients of the model and observed amplitudes are similar. In shipboard observations, the SST effect on $p\mathrm{CO}_2$ peaks from February to March, while in the eight ESMs it peaks later, from March to May.

In the top panels of Fig. 13, we show the seasonal cycles of the $p\mathrm{CO}_2$ due to the DIC effect $p\mathrm{CO}_2|_{\mathrm{DIC}}$ obtained by removing the SST effect from the $p\mathrm{CO}_2$ variations. In shipboard observations, the DIC-induced changes in $p\mathrm{CO}_2$ show a smaller north–south gradient, with about 23 μatm to the north compared to 29 μatm to the south. The observed DIC effect on $p\mathrm{CO}_2$ peaks during austral winter from July to August, about 6 months after the observed austral summer peak, due to changes

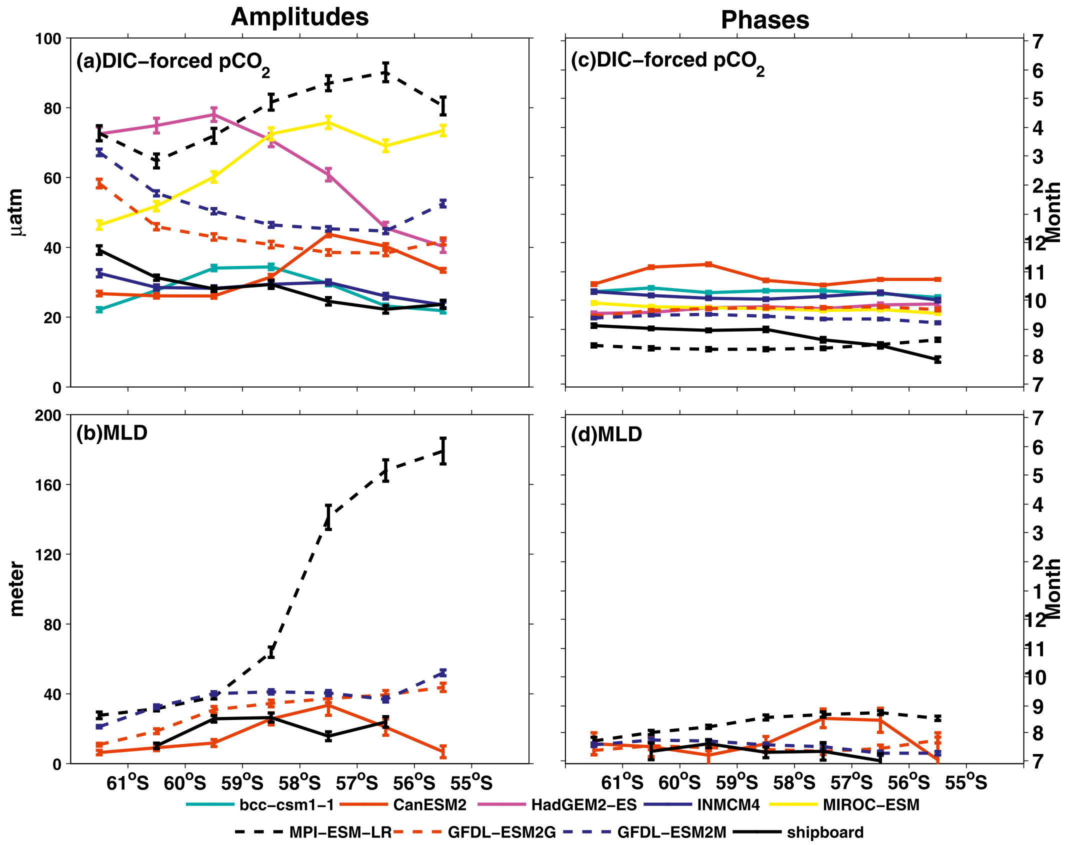

FIG. 13. (a) Amplitudes and (c) phases of the seasonal cycles of surface water $p\mathrm{CO_2}$ associated with the DIC effect for the eight CMIP5 ESMs (see legend) and the in situ measurements (black solid). (b) Amplitudes and (d) phases of the seasonal cycles of MLD for four of the CMIP5 ESMs (see legend) and the shipboard measurements (black solid). The phases indicate the peak months of the seasonal cycles of surface water $p\mathrm{CO_2}$.

in the SST effect on $p\mathrm{CO_2}$. This out-of-phase relation between the SST- and DIC-forced effects explains the small amplitudes of the seasonal cycle of $p\mathrm{CO_2}$ variations (2.5 μatm to the south and 7.5 μatm to the north; Fig. 12a), since the effects compensate for each other. The amplitudes of the eight ESMs show meridional gradients that differ from the observations, with larger magnitude seasonal cycles. The majority of the eight ESMs show peaks from July to November, about 1–2 months later than the observations.

For both the observations and the eight ESMs, the SST-forced seasonal $p\mathrm{CO_2}$ variations are approximately 6 months out of phase with DIC-forced $p\mathrm{CO_2}$ changes (Figs. 12b, 13a). As a result, the ratio of amplitudes of the seasonal $p\mathrm{CO_2}$ predicted by the SST effect to those predicted by the DIC effect indicates their relative importance in the seasonal $p\mathrm{CO_2}$ variations (Takahashi et al. 2002). Because the seasonal amplitudes have positive values in Figs. 12 and 13, their ratios also have positive signs (Fig. 14). Ratios much larger than 1 indicate a leading role for surface warming in February, and ratios much smaller than 1 indicate that DIC effects play a leading role in August. Figure 14 shows that the ratio from shipboard measurements is less than 1 (about 0.7) north of the Polar Front, suggesting that the DIC effect plays a slightly more important role than the SST effect. Because of this, the observed seawater $p\mathrm{CO_2}$ variations peak the same months as the DIC-driven $p\mathrm{CO_2}$ in August. South of the Polar Front, the SST and the DIC effects seem to play equal roles. As a result, seawater $p\mathrm{CO_2}$ peaks between October and February, in between the peak months for SST (February–March) and DIC (August–September).

Of the eight ESMs, GFDL-ESM2G and GFDL-ESM2M generally simulate realistic ratios of the seasonal SST-forced to DIC-forced $p\mathrm{CO_2}$ amplitude variations at all latitudes in the Drake Passage. The role of the DIC effect is slightly underestimated north of the Polar Front in these two models. North of the Polar Front, the ratios in three ESMs (BCC_CSM1.1, CanESM2, and HadGEM2-ES) compare well with the observations, while the DIC effect in MIROC-ESM

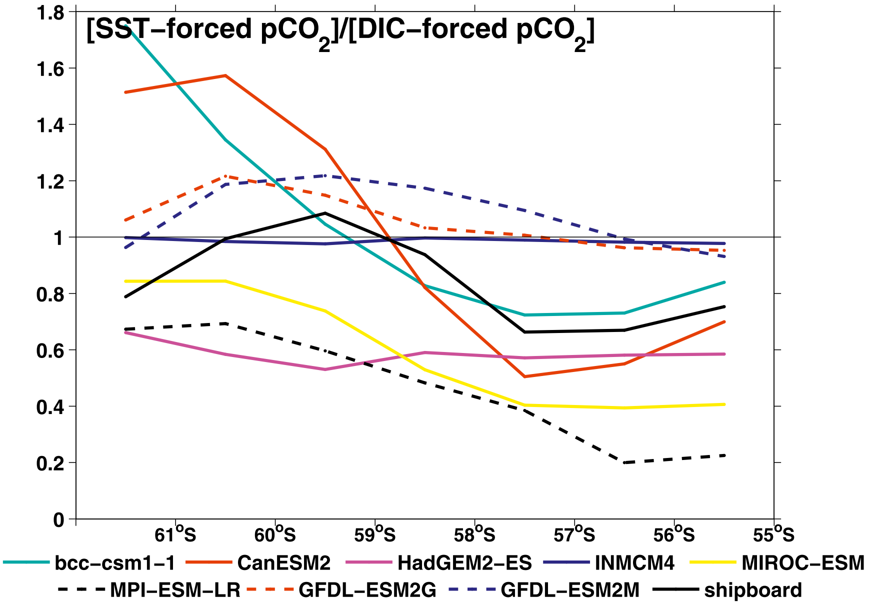

FIG. 14. The ratio of the SST-forced seasonal $p\mathrm{CO}_2$ variations to the DIC-forced seasonal $p\mathrm{CO}_2$ variations for the eight ESMs (see legend) and the shipboard measurements (black solid).

and MPI-ESM-LR seems to be overestimated in this region. South of the Polar Front, BCC_CSM1.1 and CanESM2 overestimate the role of SST while HadGEM2-ES, MIROC-ESM, and MPI-ESM-LR appear to underestimate the SST effect.

Barbero et al. (2011) found high DIC values associated with deep MLDs in the Pacific sector of the Southern Ocean. Given the important role of the seasonal DIC variations throughout the Drake Passage and to further isolate the impact of MLD on seasonal $p\mathrm{CO}_2$ variations through ocean stratification, we show the amplitudes (Fig. 13b) and phases (Fig. 13d) of the seasonal cycles of the MLD, in the shipboard measurements and four of the eight ESMs: CanESM2, MPI-ESM-LR, GFDL-ESM2G, and GFDL-ESM2M. These models are chosen because, as of July 2012, they were the only ESMs that had released MLD estimates based on the model mixing schemes. Consistent with the observed MLDs derived from the shipboard XCTD observations, the MLDs in the four ESMs peak in austral winter (July–September). Three of the ESMs (CanESM2, GFDL-ESM2G, and GFDL-ESM2M) have seasonal magnitudes that are comparable to the observations. North of the Polar Front, the amplitudes and phases of the MLD in these four ESMs seem to coincide with the DIC-induced $p\mathrm{CO}_2$ variations (Fig. 13a), suggesting the important role of the MLD variations in the seasonal $p\mathrm{CO}_2$ changes in these models. Deep MLDs of ESMs in high latitudes have also been found in the CMIP3 ESMs (Boé et al. 2009). The finding in this study also supports Boé et al.'s (2009) speculation that intermodel differences in oceanic mixing (i.e., MLDs) can be associated with a spread in the modeled oceanic uptake of CO_2. Besides MLDs, other factors, such as biological activity, also play a role in the seawater $p\mathrm{CO}_2$ seasonal variations. Cadule et al. (2010) pointed out that the phytoplankton growth rate defined by Geider et al. (1998), which is widely used in the CMIP5 ESMs, will affect the seasonality of the oceanic $p\mathrm{CO}_2$.

North of the Polar Front, MPI-ESM-LR shows a much larger seasonal cycle in MLD than the observations and the other three ESMs (CanESM2, GFDL-ESM2G, and GFDL-ESM2M), with amplitudes up to 180 m (Fig. 13b). To illustrate the spatial variations of the MLD, we show in Figs. 15a–d the July–September-mean MLD in the Drake Passage for the same ESMs as in Fig. 13b. We also show the climatological MLD derived from Argo float measurements in Fig. 15e (Holte et al. 2010). Consistent with the Argo MLD, all four ESMs show deeper MLDs north of the PF than south of the PF. While the four ESMs show different spatial features from each other, MLDs in GFDL-ESM2G and GFDL-ESM2M show the best agreement with climatology. The MPI-ESM-LR MLD in the winter can reach up to 1000 m north of the Polar Front and these deep MLDs probably play a key role in the overly large seasonal $p\mathrm{CO}_2$ variations in this model (Fig. 12a), although the causal relationship requires further study. Dunne et al. (2012) pointed out that an atmospheric air–sea surface shortwave bias may cause both seasonal MLD

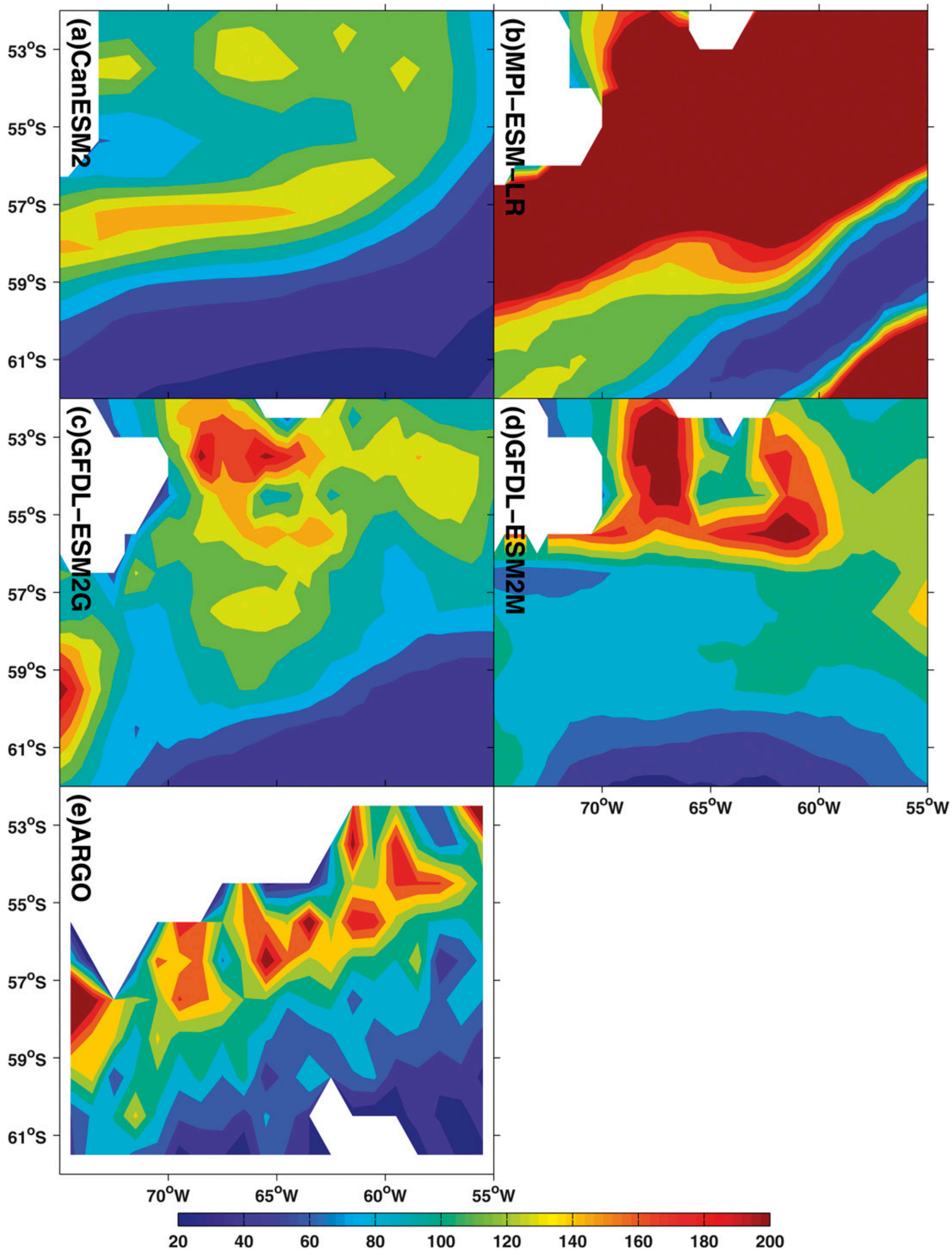

FIG. 15. July–September-mean MLDs (m), as determined from the model mixing schemes, for the Drake Passage region (50°–70°W, 52°–62°S) for (a) CanESM2, (b) MPI-ESM-LR, (c) GFDL-ESM2G, (d) GFDL-ESM2M, and (e) Argo climatology observations.

and SST biases in the Southern Ocean. Besides the variability in the biological productivity, we speculate that another possibility is that the large seasonal cycle of the MLD in MPI-ESM-LR brings CO_2 from the deep ocean to the surface layer north of the Polar Front. Because the DIC effect dominates the seasonal $p\mathrm{CO}_2$ variations north of the PF (Fig. 14), these deep MLDs seems to explain the overly large amplitudes of the seasonal cycles of the $p\mathrm{CO}_2$ variations in MPI-ESM-LR north of the Polar Front (Fig. 12a).

5. Conclusions

In this study, we have utilized the decade-long (2002–11) underway shipboard measurements from Drake Passage to examine spatial-mean, meridional (north–south), and seasonal variations in seawater $p\mathrm{CO}_2$. These year-round underway repeat measurements provide a means to assess the performance of the available CMIP5 ESMs, which for the first time directly couple the ocean carbon cycle to climate models. Our analysis has focused on assessing seawater $p\mathrm{CO}_2$ and the air-to-sea CO_2 flux in the context of winds, ocean currents, and vertical stratification in the Drake Passage. Of the eight available ESMs, six ESMs reproduce the observed annual-mean $p\mathrm{CO}_2$ values averaged over the Drake Passage region, and all ESMs but one show the significant meridional variations that are consistent with shipboard observations.

The amplitudes of seasonal cycles of the observed $p\mathrm{CO}_2$ show significant meridional variations, with the amplitude north of the Polar Front (7.5 μatm) triple the amplitude south of the Polar Front (2.5 μatm). Our analysis shows that the SST-forced and DIC-forced seawater $p\mathrm{CO}_2$ variations play an equal role south of the Polar Front, while the DIC-forced $p\mathrm{CO}_2$ variations play a slightly more important role north of the Polar Front. In addition, these two effects are out of phase at all latitudes, with the SST-forced $p\mathrm{CO}_2$ variations peaking from February to March and the DIC-forced $p\mathrm{CO}_2$ peaking from July to August. The compensation of these two effects explains the observed meridional variations of the oceanic $p\mathrm{CO}_2$. In contrast with the observations, all ESMs but INM-CM4.0 show larger seasonal cycle magnitudes at all latitudes, due to biases in the relative roles of SST-forced and DIC-forced $p\mathrm{CO}_2$ variations. North of the Polar Front, the deepening of the mixed layer in austral winter in four of the eight ESMs, possibly together with the biological consumption in the austral spring/summer (Sprintall et al. 2012), seems to play a significant role in the seasonal surface $p\mathrm{CO}_2$ variations. For ESMs that realistically simulate the seasonal deep mixed layer north of the Polar Front, the seasonal surface $p\mathrm{CO}_2$ variations compare well with observations. In contrast, ESMs with mixed layers that are too deep or too shallow north of the Polar Front directly influence surface $p\mathrm{CO}_2$ seasonal variations, because of the contribution by the vertical mixing of DIC-rich subsurface water to the surface.

Contrary to observations, which show atmospheric and surface water $p\mathrm{CO}_2$ concentrations to be near equilibrium near the Polar Front (58.5°S; 2°–4°C), in four of the eight ESMs (CanESM2, MIROC-ESM, MPI-ESM-LR, and to some extent in GFDL-ESM2G) surface water $p\mathrm{CO}_2$ values exceed atmospheric $p\mathrm{CO}_2$ values by 15–60 μatm. This causes large sea-to-air CO_2 fluxes in these four models, leading to an increase of atmospheric $p\mathrm{CO}_2$. In other words, in these ESMs the Polar Front acts as a CO_2 source to the overlying atmosphere. Because surface water $p\mathrm{CO}_2$ values far south of the Polar Front in these models are consistent with shipboard measurements, this leads to much larger gradients in seawater $p\mathrm{CO}_2$ between the -1°C water in the upwelling region and the 2°C water near the Polar Front. This implies that physical oceanic processes supply excessive $p\mathrm{CO}_2$ to the Polar Front region in these four models. This could occur as a result of strong net meridional CO_2 transport and/or overly weak subduction to the deep ocean.

Overall, compared to observations, most CMIP5 ESMs reproduce the annual-mean $p\mathrm{CO}_2$ values averaged in the Drake Passage region. However, there remain several distinct discrepancies. The ESMs typically show much larger seasonal cycles than the shipboard measurements. Other issues include excessive surface water $p\mathrm{CO}_2$ concentrations near the Polar Front, strong equatorward Ekman currents driven by the overly intensified westerlies, strong net equatorward meridional currents owing to weak poleward eddy transport that is insufficient to compensate the equatorward Ekman currents, excessively strong vertical stratification, and winter mixed layers that are either too deep or too shallow north of the Polar Front. We hypothesize that within the Drake Passage region these models release too much CO_2 to the overlying atmosphere, which reduces the inventory of DIC in the model Drake Passage. Further studies will be needed to examine whether the processes in Drake Passage are representative of the entire Southern Ocean and further whether these processes significantly impact the atmospheric CO_2 concentrations in the ESM projections.

The underway shipboard $p\mathrm{CO}_2$ measurements used in this study provide a valuable benchmark for assessing the performance of the CMIP5 ESMs in the Drake Passage. However, the sparse in situ measurements prohibit us from examining zonal (east–west) variations of the surface ocean $p\mathrm{CO}_2$ throughout the whole Southern Ocean. Lenton et al. (2012) analyzed the growth rate of the seawater $p\mathrm{CO}_2$ across the ACC system and found that different mechanisms influence the surface ocean $p\mathrm{CO}_2$ in the Atlantic compared to the Pacific–Indian sectors. In this study, we found the spatially averaged sea-to-air CO_2 flux and seasonal $p\mathrm{CO}_2$ variations in the entire circumpolar region (56°–62°S) agree well with their variations in the Drake Passage for most of the eight ESMs. In addition, the ESM $p\mathrm{CO}_2$ anomalies (removing the annual mean, long-term trend, and seasonal cycles) in Drake Passage significantly correlate with the other areas of the Southern Ocean. Thus, despite the limited zonal spatial coverage in the Drake Passage measurements, they appear to provide a useful means to assess the representation of CO2 in long-term climate projections.

Acknowledgments. We gratefully acknowledge support from the National Science Foundation (OCE Award 0850350 and Office of Polar Programs Awards 0943818, 1129005, and 0944761) and NASA Award NNX08AR63G. Jiang was supported as a part of a diagnostic analysis effort proposed by U.S. CLIVAR (OPP Award 1129005) and by the Scripps Postdoctoral fellowship and NASA Award NNX08AR63G. The authors would like to acknowledge Teresa K. Chereskin and Sharon Escher for providing the LMG datasets. We also thank all the technical and scientific support from the staff of eight ESM groups and the Program for Climate Model Diagnostic and Intercomparison (PCMDI) for making the ESM output available to the public. Jiang would like to acknowledge Dr. François W. Primeau for his constructive and valuable comments during her stay at University of California, Irvine. She would also like to thank Camisa Carlson at Earth & Space Research for her thorough English language editing. The authors thank three anonymous reviewers and the editor for their insightful and constructive comments and suggestions. Q-COAPS was obtained online (from http://coaps.fsu.edu/scatterometry/gridded/). The OSCAR ocean current data from the Physical Oceanography Distributed Active Archive Center (PO.DAAC) at the NASA Jet Propulsion Laboratory, Pasadena, California, was obtained online (from ftp://podaac.jpl.nasa.gov/).

REFERENCES

Antonov, J. I., and Coauthors, 2010: *Salinity.* Vol. 2, *World Ocean Atlas 2009,* NOAA Atlas NESDIS 69, 44 pp.

Arora, V. K., and Coauthors, 2011: Carbon emission limits required to satisfy future representative concentration pathways of greenhouse gases. *Geophys. Res. Lett.,* **38,** L05805, doi:10.1029/2010GL046270.

Barbero, L., J. Boutin, L. Merlivat, N. Martin, T. Takahashi, S. C. Sutherland, and R. Wanninkhof, 2011: Importance of water mass formation regions for the air-sea CO_2 flux estimate in the Southern Ocean. *Global Biogeochem. Cycles,* **25,** GB1005, doi:10.1029/2010GB003818.

Boé, J., A. Hall, and X. Qu, 2009: Deep ocean heat uptake as a major source of spread in transient climate change simulations. *Geophys. Res. Lett.,* **36,** L22701, doi:10.1029/2009GL040845.

Böning, C. W., A. Dispert, M. Visbeck, S. R. Rintoul, and F. U. Schwarzkopf, 2008: The response of the Antarctic Circumpolar Current to recent climate change. *Nat. Geosci.,* **1,** 864–869.

Bonjean, F., and G. Lagerloef, 2002: Diagnostic model and analysis of the surface currents in the tropical Pacific Ocean. *J. Phys. Oceanogr.,* **32,** 2938–2954.

Cadule, P., P. Friedlingstein, L. Bopp, S. Sitch, C. D. Jones, P. Ciais, S. L. Piao, and P. Peylin, 2010: Benchmarking coupled climate-carbon models against long-term atmospheric CO_2 measurements. *Global Biogeochem. Cycles,* **24,** GB2016, doi:10.1029/2009GB003556.

Christian, J. R., and Coauthors, 2010: The global carbon cycle in the Canadian Earth System Model (CanESM1): Preindustrial control simulation. *J. Geophys. Res.,* **115,** G03014, doi:10.1029/2008JG000920.

Collins, W. J., and Coauthors, 2011: Development and evaluation of an Earth-system model—HadGEM2. *Geosci. Model Dev.,* **4,** 1051–1077.

Conway, T. J., P. P. Tans, L. S. Waterman, K. W. Thoning, D. R. Kitzis, K. A. Masarie, and N. Zhang, 1994: Evidence of interannual variability of the carbon cycle from the NOAA/CMDL global air sampling network. *J. Geophys. Res.,* **99,** 22 831–22 855.

Cox, P., P. Friedlingstein, and P. Rayner, 2002: Modelling climate-carbon cycle feedbacks: A cross disciplinary collaboration priority. *IGBP Global Change Newsletter,* No. **49,** IGBP Secretariat, Stockholm, Sweden, 12–14.

Dohan, K., and N. Maximenko, 2010: Monitoring ocean currents with satellite sensors. *Oceanography,* **23,** 94–103.

——, and Coauthors, 2010: Measuring the global ocean surface circulation with satellite and in situ observations. *Proc. OceanObs'09: Sustained Ocean Observations and Information for Society,* Venice, Italy, European Space Agency, WPP-306.

Downes, S. M., A. Gnanadesikan, S. M. Griffies, and J. L. Sarmiento, 2011: Water mass exchange in the Southern Ocean in coupled climate models. *J. Phys. Oceanogr.,* **41,** 1756–1771.

Dunne, J. P., and Coauthors, 2012: GFDLs ESM2 global coupled climate–carbon Earth system models. Part I: Physical formulation and baseline simulation characteristics. *J. Climate,* **25,** 6646–6665.

——, and Coauthors, 2013: GFDL's ESM2 global coupled climate–carbon Earth system models. Part II: Carbon system formulation and baseline simulation characteristics. *J. Climate,* **26,** 2247–2267.

Ferrari, R., S. Griffies, A. Nurser, and G. Vallis, 2010: A boundary value problem for the parameterized mesoscale eddy transport. *Ocean Modell.,* **32,** 143–156.

Friedlingstein, P., and Coauthors, 2006: Climate–carbon cycle feedback analysis: Results from the C^4MIP model intercomparison. *J. Climate,* **19,** 3337–3353.

Fung, I., P. Rayner, and P. Friedlingstein, 2000: Full-form earth system models: Coupled carbon-climate interaction experiment (the flying leap). *IGBP Global Change Newsletter,* No. 41, IGBP Secretariat, Stockholm, Sweden, 7–8.

Geider, R. J., H. L. MacIntyre, and T. M. Kana, 1998: A dynamic regulatory model of phytoplanktonic acclimation to light, nutrients, and temperature. *Limnol. Oceanogr.,* **43,** 679–694.

Gent, P. R., and J. C. McWilliams, 1990: Isopycnal mixing in ocean general circulation models. *J. Phys. Oceanogr.,* **20,** 150–155.

Gille, S. T., 2008: Decadal-scale temperature trends in the Southern Hemisphere ocean. *J. Climate,* **21,** 4749–4765.

Gnanadesikan, A., and Coauthors, 2006: GFDL's CM2 global coupled climate models. Part II: The baseline ocean simulation. *J. Climate,* **19,** 675–697.

Griffies, S. M., 1998: The Gent–McWilliams skew flux. *J. Phys. Oceanogr.,* **28,** 831–841.

Holte, J., and L. Talley, 2009: A new algorithm for finding mixed layer depths with applications to Argo data and Subantarctic

Mode Water formation. *J. Atmos. Oceanic Technol.,* **26,** 1920–1939.

——, J. Gilson, L. Talley, and D. Roemmich, cited 2010: Argo mixed layers. Scripps Institution of Oceanography/UCSD. [Available online at http://mixedlayer.ucsd.edu/.]

Ilyina, T., K. D. Six, J. Segschneider, E. Maier-Reimer, H. Li, and I. Nùñez-Riboni, 2013: Global ocean biogeochemistry model HAMOCC: Model architecture and performance as component of the MPI-Earth system model in different CMIP5 experimental realizations. *J. Adv. Model. Earth Syst.,* **5,** 287–315, doi:10.1029/2012MS000178.

Ito, T., M. Woloszyn, and M. Mazloff, 2009: Anthropogenic carbon dioxide transport in the Southern Ocean driven by Ekman flow. *Nature,* **463,** 80–83.

Iudicone, D., K. B. Rodgers, I. Stendardo, O. Aumont, G. Madec, L. Bopp, O. Mangoni, and M. Ribera d'Alcala, 2011: Water masses as a unifying framework for understanding the Southern Ocean carbon cycle. *Biogeosciences,* **8,** 1031–1052.

Jiang, C., S. T. Gille, J. Sprintall, K. Yoshimura, and M. Kanamitsu, 2012: Spatial variation in turbulent heat fluxes in Drake Passage. *J. Climate,* **25,** 1470–1488.

Johns, T. C., and Coauthors, 2006: The new Hadley Centre climate model (HadGEM1): Evaluation of coupled simulations. *J. Climate,* **19,** 1327–1353.

Jones, C. D., and Coauthors, 2011a: The HadGEM2-ES implementation of CMIP5 centennial simulations. *Geosci. Model Dev.,* **4,** 543–570.

Jones, D. C., T. Ito, and N. S. Lovenduski, 2011b: The transient response of the Southern Ocean pycnocline to changing atmospheric winds. *Geophys. Res. Lett.,* **38,** L15604, doi:10.1029/2011GL048145.

Lagerloef, G. S. E., G. T. Mitchum, R. B. Lukas, and P. P. Niiler, 1999: Tropical Pacific near-surface currents estimated from altimeter, wind, and drifter data. *J. Geophys. Res.,* **104,** 23 313–23 326.

Lenton, A., and Coauthors, 2012: The observed evolution of oceanic pCO_2 and its drivers over the last two decades. *Global Biogeochem. Cycles,* **26,** GB2021, doi:10.1029/2011GB004095.

Le Quéré, C., and Coauthors, 2007: Saturation of the Southern Ocean CO_2 sink due to recent climate change. *Science,* **316,** 1735–1738.

Liss, P. S., and L. Merlivat, 1986: Air-sea gas exchange rates: introduction and synthesis. *The Role of Air-Sea Exchange in Geochemical Cycling,* P. Buat-Menard, Ed., D. Reidel, 113–127.

Locarnini, R. A., A. V. Mishonov, J. I. Antonov, T. P. Boyer, H. E. Garcia, O. K. Baranova, M. M. Zweng, and D. R. Johnson, 2010: *Temperature.* Vol. 1, *World Ocean Atlas 2009,* NOAA Atlas NESDIS 68, 52 pp.

Lovenduski, N. S., N. Gruber, S. C. Doney, and I. D. Lima, 2007: Enhanced CO_2 outgassing in the Southern Ocean from a positive phase of the southern annular mode. *Global Biogeochem. Cycles,* **21,** GB2026, doi:10.1029/2006GB002900.

——, ——, and ——, 2008: Toward a mechanistic understanding of the decadal trends in the Southern Ocean carbon sink. *Global Biogeochem. Cycles,* **22,** GB3016, doi:10.1029/2007GB003139.

Lumpkin, R., and M. Pazos, 2007: Measuring surface currents with surface velocity program drifters: The instrument, its data, and some recent results. *Lagrangian Analysis and Prediction of Coastal and Ocean Dynamics (LAPCOD),* A. Griffa et al., Eds., Cambridge University Press, 39–67.

Marinov, I., A. Gnanadesikan, R. Toggweiler, and J. L. Sarmiento, 2006: The Southern Ocean biogeochemical divide. *Nature,* **441,** 964–967.

——, ——, J. L. Sarmiento, J. R. Toggweiler, M. Follows, and B. K. Mignone, 2008: Impact of oceanic circulation on the biological carbon storage in the ocean and atmospheric pCO_2. *Global Biogeochem. Cycles,* **22,** GB3007, doi:10.1029/2007GB002958.

Marsland, S. J., H. Haak, J. H. Jungclaus, M. Latif, and F. Roske, 2003: The Max-Planck-Institute global ocean/sea ice model with orthogonal curvilinear coordinates. *Ocean Modell.,* **5,** 91–127.

McNeil, B. I., N. Netzl, R. M. Key, R. J. Matear, and A. Corbiere, 2007: An empirical estimate of the Southern Ocean air-sea CO_2 flux. *Global Biogeochem. Cycles,* **21,** GB3011, doi:10.1029/2007GB002991.

Mikaloff Fletcher, S. E., and Coauthors, 2006: Inverse estimates of anthropogenic CO_2 uptake, transport, and storage by the ocean. *Global Biogeochem. Cycles,* **20,** GB2002, doi:10.1029/2005GB002530.

——, and Coauthors, 2007: Inverse estimates of the oceanic sources and sinks of natural CO_2 and the implied oceanic carbon transport. *Global Biogeochem. Cycles,* **21,** GB1010, doi:10.1029/2006GB002751.

Orr, J. C., and Coauthors, 2001: Estimates of anthropogenic carbon uptake from four three-dimensional global ocean models. *Global Biogeochem. Cycles,* **15,** 43–60.

Pegion, P., M. Bourassa, D. M. Legler, and J. J. O'Brien, 2000: Objectively derived daily "winds" from satellite scatterometer data. *Mon. Wea. Rev.,* **128,** 3150–3168.

Raddatz, T. J., and Coauthors, 2007: Will the tropical land biosphere dominate the climate-carbon cycle feedback during the twenty-first century? *Climate Dyn.,* **29,** 565–574.

Reynolds, R. W., and T. M. Smith, 1994: Improved global sea surface temperature analysis using optimum interpolation. *J. Climate,* **7,** 929–948.

Russell, J. L., K. W. Dixon, A. Gnanadesikan, R. J. Stouffer, and J. R. Toggweiler, 2006: The Southern Hemisphere westerlies in a warming world: Propping open the door to the deep ocean. *J. Climate,* **19,** 6382–6390.

Sarmiento, J. L., and N. Gruber, 2006: *Ocean Biogeochemical Dynamics.* Princeton University Press, 503 pp.

——, and Coauthors, 2004: Response of ocean ecosystems to climate warming. *Global Biogeochem. Cycles,* **18,** GB3003, doi:10.1029/2003GB002134.

Speer, K., S. R. Rintoul, and B. Sloyan, 2000: The diabatic Deacon cell. *J. Phys. Oceanogr.,* **30,** 3212–3222.

Sprintall, J., 2003: Seasonal to interannual upper-ocean variability in the Drake Passage. *J. Mar. Res.,* **61,** 27–57.

——, T. Chereskin, and C. Sweeney, 2012: High-resolution underway upper ocean and surface atmospheric observations in Drake Passage: Synergistic measurements for climate science. *Oceanography,* **25,** 70–82.

Stephenson, G. R., S. T. Gille, and J. Sprintall, 2012: Seasonal variability of upper ocean heat content in Drake Passage. *J. Geophys. Res.,* **117,** C04019, doi:10.1029/2011JC007772.

Swart, N. C., and J. C. Fyfe, 2011: Ocean carbon uptake and storage influenced by wind bias in global climate models. *Nat. Climate Change,* **2,** 47–52.

Sweeney, C., E. Gloor, A. R. Jacobson, R. M. Key, G. McKinley, J. L. Sarmiento, and R. Wanninkhof, 2007: Constraining global air-sea gas exchange for CO_2 with recent bomb ^{14}C measurements. *Global Biogeochem. Cycles,* **21,** GB2015, doi:10.1029/2006GB002784.

Takahashi, T., J. Olafsson, J. G. Goddard, D. W. Chipman, and S. C. Sutherland, 1993: Seasonal variation of CO_2 and nutrients in the high-latitude surface oceans: A comparative study. *Global Biogeochem. Cycles,* **7,** 843–878.

——, and Coauthors, 2002: Global sea–air CO_2 flux based on climatological surface ocean pCO_2, and seasonal biological and temperature effects. *Deep-Sea Res. II,* **49,** 1601–1622.

——, and Coauthors, 2009: Climatological mean and decadal change in surface ocean pCO_2, and net sea-air CO_2 flux over the global oceans. *Deep-Sea Res. II,* **56,** 554–557, doi:10.1016/j.dsr2.2008.12.009; Corrigendum, *Deep-Sea Res. I,* **56,** 2075–2076, doi:10.1016/j.dsr.2009.07.007.

Taylor, K. E., R. J. Stouffer, and G. A. Meehl, 2012: An overview of CMIP5 and the experiment design. *Bull. Amer. Meteor. Soc.,* **93,** 485–498.

Toggweiler, J. R., and B. Samuels, 1995: Effect of Drake Passage on the global thermohaline circulation. *Deep-Sea Res.,* **42I,** 477–500.

Volodin, E. M., N. A. Dianskii, and A. V. Gusev, 2010: Simulating present-day climate with the INMCM4.0 coupled model of the atmospheric and oceanic general circulations. *Izv. Atmos. Ocean. Phys.,* **46,** 414–431.

Wanninkhof, R., and W. M. McGillis, 1999: A cubic relationship between gas transfer and wind speed. *Geophys. Res. Lett.,* **26,** 1889–1892.

Watanabe, S., and Coauthors, 2011: MIROC-ESM 2010: Model description and basic results of CMIP5-20c3m experiments. *Geosci. Model Dev.,* **4,** 845–872.

Woloszyn, M., M. Mazloff, and T. Ito, 2011: Testing an eddy-permitting model of the Southern Ocean carbon cycle against observations. *Ocean Modell.,* **39,** 170–182.

Wu, T., and Coauthors, 2013: Global carbon budgets simulated by the Beijing Climate Center Climate System Model for the last century. *J. Geophys. Res.,* **118,** 4326–4347, doi:10.1002/jgrd.50320.

Zahariev, K., J. Christian, and K. Denman, 2008: Preindustrial, historical, and fertilization simulations using a global ocean carbon model with new parameterizations of iron limitation, calcification, and N_2 fixation. *Prog. Oceanogr.,* **77,** 56–82.